

AperTO - Archivio Istituzionale Open Access dell'Università di Torino

Sensitivity of the thermohaline circulation during the Messinian: Toward constraining the dynamics of Mediterranean deoxygenation

This is the author's manuscript

Original Citation:

Availability:

This version is available <http://hdl.handle.net/2318/1952069> since 2024-04-05T07:36:38Z

Published version:

DOI:10.1016/j.dsr.2023.104217

Terms of use:

Open Access

Anyone can freely access the full text of works made available as "Open Access". Works made available under a Creative Commons license can be used according to the terms and conditions of said license. Use of all other works requires consent of the right holder (author or publisher) if not exempted from copyright protection by the applicable law.

(Article begins on next page)

Journal Pre-proof



Sensitivity of the thermohaline circulation during the Messinian: Toward constraining the dynamics of Mediterranean deoxygenation

A.M. Mancini, R. Gennari, F. Lozar, M. Natalicchio, G. Della Porta, D. Bernasconi, L. Pellegrino, F. Dela Pierre, L. Martire, A. Negri

PII: S0967-0637(23)00256-X

DOI: <https://doi.org/10.1016/j.dsr.2023.104217>

Reference: DSRI 104217

To appear in: *Deep-Sea Research Part I*

Received Date: 25 August 2023

Revised Date: 16 November 2023

Accepted Date: 13 December 2023

Please cite this article as: Mancini, A.M., Gennari, R., Lozar, F., Natalicchio, M., Della Porta, G., Bernasconi, D., Pellegrino, L., Dela Pierre, F., Martire, L., Negri, A., Sensitivity of the thermohaline circulation during the Messinian: Toward constraining the dynamics of Mediterranean deoxygenation, *Deep-Sea Research Part I* (2024), doi: <https://doi.org/10.1016/j.dsr.2023.104217>.

This is a PDF file of an article that has undergone enhancements after acceptance, such as the addition of a cover page and metadata, and formatting for readability, but it is not yet the definitive version of record. This version will undergo additional copyediting, typesetting and review before it is published in its final form, but we are providing this version to give early visibility of the article. Please note that, during the production process, errors may be discovered which could affect the content, and all legal disclaimers that apply to the journal pertain.

© 2023 Published by Elsevier Ltd.

1 Sensitivity of the Thermohaline Circulation during the Messinian: Toward

2 Constraining the Dynamics of Mediterranean Deoxygenation

3 Mancini^a, A.M., Gennari^a, R., Lozar^a, F., Natalicchio^a, M., Della Porta^b, G., Bernasconi^a, D., Pellegrino^a, L., Dela Pierre^a,
4 F., Martire^a, L., Negri^c, A.

5 ^a Earth Sciences Department, Università degli Studi di Torino, 10125 Torino, Italy

6 ^b "Earth Sciences Department "A. Desio", Università degli Studi di Milano, 20133 Milan, Italy

7
8 ^c Department of Life and Environmental Science, Università Politecnica delle Marche, 60122 Ancona, Italy

9

10

11

12

13

14

13 Abstract

14

15

16

17

18

19

20

21

22

23

24

25

26

27

28

29

30

31

32

33

34

35

36

37

38

During the Messinian, the sensitivity of the Mediterranean Basin to ecosystem perturbation was enhanced in response to the progressive restriction of water exchange with the Atlantic Ocean. The widespread deposition of organic-rich layers (i.e. sapropel) during the Messinian testifies the perturbation of the carbon and oxygen cycles; indeed, these sediments were deposited under conditions of oxygen starvation, presumably in response to a periodic deterioration of the thermohaline circulation strength. Disentangling the causes, the effect and magnitude of the thermohaline circulation weakening during the geological past is crucial for better constraining present and near-future deoxygenation dynamics in the Mediterranean region under the current climate warming. For this purpose, we investigate a Messinian sapropel-bearing succession cropping out at Monte dei Corvi (Ancona, central Italy) with mineralogical, petrographic, micropaleontological and stable Carbon and Oxygen isotopic analyses. We show that sapropel layers were deposited in response to an increase of the sea surface buoyancy, which hampered the thermohaline circulation and thus the oxygenation of bottom water, in turn affecting the bioturbating organisms. Within the lithological cycle, the recovery of an efficient thermohaline circulation is recorded by thin packstone layers underlying the marly limestone/marlstone, which record intense bottom currents. The marly limestone/marlstone accumulated during periods of intense primary productivity and organic carbon export to the sea bottom, which promoted bottom hypoxia but not organic matter preservation. We infer that these lithological changes resulted from variations in the Adriatic Deep Water formation system, controlled by precession-driven climatic and oceanographic changes.

By integrating previously published Sea Surface Temperature (SST) with new isotopic and mineralogical data, we show that variations in Sea Surface Salinity (SSS) were the leading factor controlling sapropel deposition, minimizing the role of primary productivity. The SSTs characterizing the sapropel deposits are close to the range of those projected in the Eastern Mediterranean at the end of this century under climate warming. In this scenario, future warming will be coupled with SSS increase, which will counteract the density loss provided by temperature, making the bottom deoxygenation in the Eastern Mediterranean

39 abysses unlikely. However, additional forcing, such as winter heat waves and eutrophication, could
40 contribute to negatively affecting the Mediterranean oxygen balance and should be considered in model-
41 based projections.

42

43 Introduction

44 The Mediterranean region is considered one of the most sensitive regions to climate change on Earth; for
45 this reason it has been referred to as a climate change “hot-spot” (Giorgi, 2006). Warming and drying were
46 recorded during the last decades and these trends are projected to further exacerbate in the next future
47 (IPCC, 2021). The warming trend is impacting the thermohaline circulation strength (Somot et al., 2006),
48 with possible repercussions on the oxygen renewal in the deep-water masses (Diaz and Rosemberg, 2008).
49 The Mediterranean thermohaline circulation mostly relies on cold wind stress and evaporation
50 mechanisms; the lighter (less saline but colder) surface water entering the Gibraltar Strait and flowing
51 toward the Eastern Mediterranean progressively becomes saltier and warmer. In the Levantine Basin
52 during winter the cold and dry wind decreases the temperature and increases the salinity of surface water,
53 favoring vertical convection and the formation of the Levantine Intermediate Water (LIW), which flows
54 west-ward between 150 - 600 meter depth (Rohling et al., 2015 and reference therein). Similarly, in the
55 Northern Adriatic, the winter cold wind decreases the temperature of surficial waters favoring their sink;
56 this cold water flows south-ward at the Adriatic bottom and is mixed with the LIW that comes from the
57 Otranto Sill (Rohling et al., 2015). The mixing between these two water masses promotes the formation of
58 the Adriatic Deep Water (ADW), which resides below the LIW and represents the major contribution of
59 deep-water renewal in the Eastern Mediterranean abysses, assuring oxygen supply at the bottom.

60 Starting from the Langhian (Taylforth et al., 2014; Athanasiou et al., 2021), the Mediterranean experienced
61 deoxygenation events related to a strong reduction, or even a complete stop, of the thermohaline
62 circulation (Stratford et al., 2000; De Lange et al., 2008; Rohling et al., 2015), coupled with an increase in
63 marine primary productivity (Rohling et al., 2015; Blanchet et al., 2021). These paleoceanographic changes
64 caused most of the deoxygenation events in the geological history of the Mediterranean and were mostly
65 related to changes in continental runoff, temperature and sea level (Rohling et al., 2015 and reference
66 therein). A strong temporal correlation exists between the Mediterranean deoxygenation events and
67 precession minima/eccentricity maxima, since these orbital parameters control the incoming solar energy
68 and promote the northward migration of the monsoon rain belt over North Africa, therefore increasing
69 fluvial discharge in the Eastern Mediterranean Basin mostly through the Nile River (Rossignol-Strick et al.,
70 1982; Hennekam et al., 2014; Rohling et al., 2015). The enhanced freshwater input into the Mediterranean
71 Basin increased the buoyancy of surface waters, thus promoting density stratification of the water column

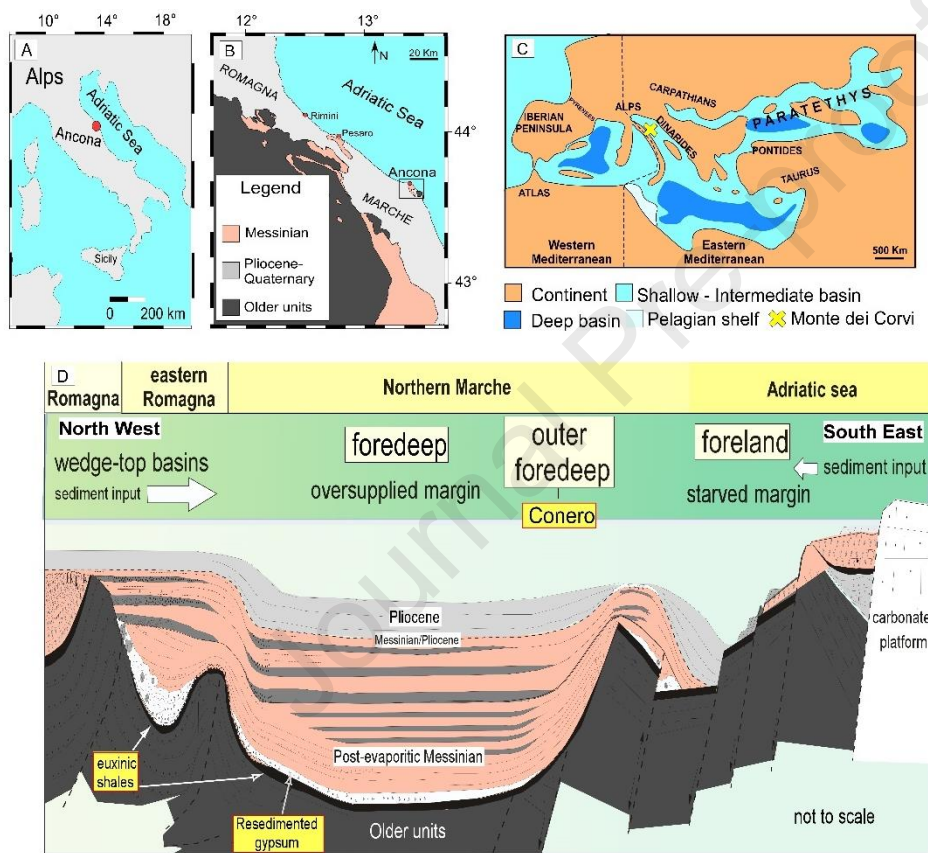
72 and hampering deep water renewal (Rohling et al., 2015). These events are recorded by dark layers, termed
73 sapropels, which are marine sediments enriched in organic carbon (Kidd et al., 1978), which punctuated the
74 Eastern Mediterranean sedimentary record of the last 15 My (Taylforth et al., 2014; Athanasiou et al.,
75 2021). Sapropel deposition was induced by sharp perturbations of the oxygen and carbon cycles; indeed,
76 these layers record organic matter preservation in response to bottom oxygen deficiency. During the
77 Messinian, sapropel deposits are more widespread and frequent with respect to the rest of the
78 Mediterranean geological record, because the tectonic shallowing of the paleo-Gibraltar gateway reduced
79 the water exchange with the Atlantic Ocean (Roveri et al., 2014; Flecker et al., 2015) and increased the
80 sensitivity of thermohaline circulation to freshwater input, hence promoting the weakening of the
81 thermohaline circulation and bottom oxygen delivery (Kouwenhoven and Van der Zwaan, 2006; Mancini et
82 al., 2020; Bulian et al., 2022). The freshwater input from the African rivers was coupled with the Paratethys
83 freshwater spill (Gladstone et al., 2007), which further enhanced the density loss of surface water during
84 precession minima in the Eastern Mediterranean. These characteristics make the Messinian sedimentary
85 succession an excellent case study for unraveling the causes and the effects of deoxygenation events in the
86 geological past and for comparing such past environmental perturbations with the current and near-future
87 scenarios of climate change.

88 A sapropel-bearing Messinian succession exposed in the Northern Apennines (Conero Riviera, Ancona,
89 Italy) is investigated using a high-resolution multidisciplinary approach, encompassing mineralogical,
90 sedimentological, micropaleontological, and carbonate stable Oxygen and Carbon isotope data. The
91 objective is to unravel the environmental conditions responsible for Messinian sapropel deposition in the
92 Adriatic Basin and compare these past perturbations with those projected in the near future under the
93 influence of climate change scenarios in the Mediterranean Basin.

94 **2. Geological setting**

95 The studied section is located south of Ancona and is exposed along the shoreline between Monte dei Corvi
96 and Mezzavalle beach (43° 34'N, 13° 34'E; Fig. 1). This area pertains to the central sector of the modern
97 foredeep basin and foreland ramp of the northern Apennine belt (Roveri et al., 2005). The sedimentary
98 succession is almost continuous from the Aquitanian to the Messinian (Hilgen et al., 2003). The Messinian
99 succession was deposited in the outer northern Apennine foredeep (Roveri et al., 2005) and is composed of
100 a pre-evaporitic, a syn-evaporitic and a post-evaporitic unit (Roveri et al., 2005; Iaccarino et al., 2008). The
101 ~ 20 m thick pre-evaporitic unit is referred to as the "Euxinic shale interval" and shows a precession-driven
102 cyclic stacking pattern evidenced by couplets of dark, organic-rich marlstone (here referred as sapropel)
103 and white/light grey limestone or marlstone (Hüsing et al., 2009; Di Stefano et al., 2010). This interval was
104 deposited at a water depth of 300-400 m (outer shelf/upper slope, Iaccarino et al., 2008) and was
105 characterized by hemipelagic sedimentation in the outer foredeep setting (Fig. 1; Roveri et al., 2005). The

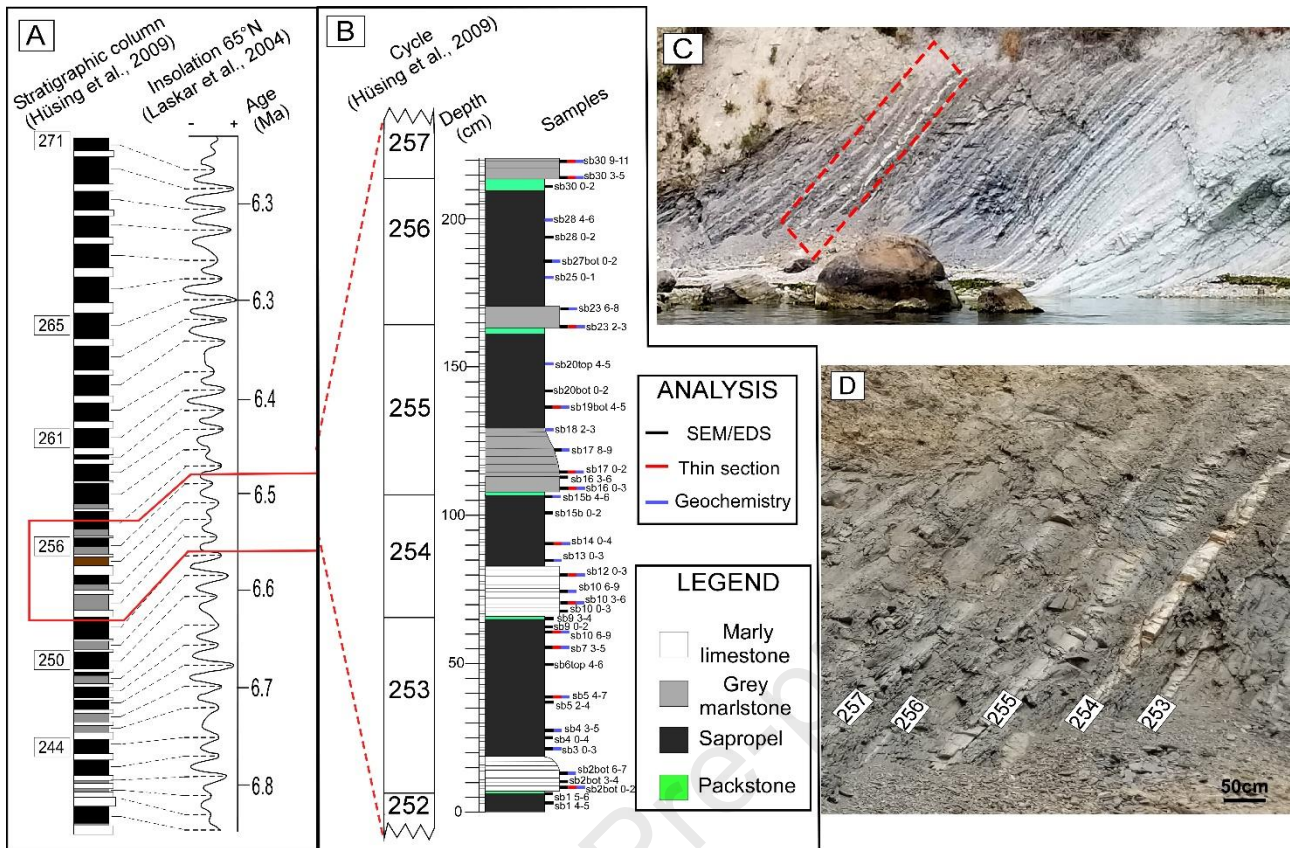
106 syn-evaporitic unit is represented by resedimented gypsum deposits partially covered by a landslide that is
 107 overlain by ~ 170 m of post-evaporitic deposits (Bertini, 2006). The Messinian succession ends with a
 108 complex biocalcarenic sedimentary body, termed Trave, which marks the transition to the Pliocene
 109 sediments. The studied section pertains to the pre-evaporitic Messinian “Euxinic shale interval” and was
 110 referred to as “extension Monte dei Corvi Beach” in previous studies (Hüsing et al., 2009; Di Stefano et al.,
 111 2010). The age model proposed by Hüsing et al. (2009) was applied, which has been defined according to
 112 biostratigraphic, magnetostratigraphic and cyclostratigraphic data. For this study, 4 lithological cycles (from
 113 253 to 256 according to Hüsing et al., 2009) were analyzed, with an inferred age of 6.553 to 6.479 Ma. A
 114 total of 40 samples were collected, with a mean stratigraphic spacing of 5 cm (Fig. 2).



115
 116 Fig.1: Geological and paleogeographic map of the studied area and general stratigraphic scheme of the late Neogene deposits.
 117 A and B: Location and simplified geological map of the studied area. The studied section is indicated by the black square in B.
 118 C: Paleogeographic reconstruction of the Mediterranean during the early Messinian. Modified after Popov et al. (2004).
 119 D: Stratigraphic architecture of the Messinian deposits of the Apennine foredeep with location of the studied area (Conero).
 120 Modified after Roveri et al. (2005).

121

122



123

124

125

126

127

128

129

3-Materials and Methods

130

3.1 Petrographical, geochemical and micropaleontological analyses

131

132

133

134

135

136

137

138

139

140

141

142

Fig.2. A: Stratigraphic column of Monte dei Corvi section; numbers on the left refer to the identified cycles (after Hüsing et al., 2009); The red polygon shows the studied part of the section. B: The studied part of the section with detail on lithology and sample position. C: Outcrop view of the section showing the sampled interval (red dashed line square). D: Close-up of the studied section with labeling of the cycles.

Among the 40 samples collected, thirteen polished thin sections were prepared for optical and cathodoluminescence microscope analyses; a CITL 8200 mk3 equipment operated at 15-17 kV and 350-500 mA was used. Scanning Electron Microscope (SEM) and energy-dispersive X-ray spectroscopy (EDS) analyses were performed on the same carbon-coated thin sections for semiquantitative elemental analyses and backscattered electron imagery (BSEI) using a JSM-IT300LV equipped with EDS Oxford Instruments Link Systems (Department of Earth Sciences, University of Turin). Elemental compositional maps were obtained from selected areas using the software Inca. SEM analyses were also performed on 36 freshly broken chips for morphological investigations, along with a qualitative micropaleontological observation (Fig. 2) to estimate the abundance and preservation of benthic and planktic foraminifers and calcareous nannofossils. Four standard smear slides were prepared and quantitatively investigated to assess the calcareous nannofossil assemblages. These samples were observed at the optical microscope at 1250x and at least 400 specimens were identified for the calculation of the relative abundance.

143 Carbon ($\delta^{13}\text{C}$) and Oxygen ($\delta^{18}\text{O}$) stable isotope analyses were conducted on 26 powdered samples (Fig. 2)
144 using an automated carbonate preparation device (Gasbench II) and a Thermo Fisher Scientific Delta V
145 Advantage continuous flow mass spectrometer at the University of Milan. The powders were reacted with
146 >99% orthophosphoric acid at 25° and 70° C with the aim to distinguish the possible contribution of the
147 different carbonate minerals (calcite and dolomite). Carbon and oxygen isotope values are expressed in the
148 conventional delta notation calibrated to the Vienna Pee-Dee Belemnite (V-PDB) scale by the international
149 standards IAEA 603 and NBS-18. Analytical reproducibility was better than $\pm 0.1\text{‰}$ for both $\delta^{18}\text{O}$ and $\delta^{13}\text{C}$
150 values. In order to highlight differences in the isotopic composition between bulk calcite and calcareous
151 nanofossils calcite, 4 samples (sb2bot 0-2; sb2bot 6-7; sb10 6-7; sb17 8-9; Fig. 2) were gently crushed to
152 obtain ~ 1 mm of grain-size, the powder and grains obtained were successively sieved at 45 μm in order to
153 concentrate the calcareous nanofossils, in agreement with previous paleoceanographic studies (Anderson
154 and Steinmetz, 1981; Steinmetz, 1994, among others). Successively, the fraction $<45 \mu\text{m}$ was analyzed with
155 the same procedure applied to the bulk sediment. These samples were chosen because their assemblages
156 show a different taxonomic diversity (see paragraph 4.1).

157 The Total Organic Carbon (TOC, wt%) content was obtained from 10 powdered samples that were first
158 reacted with HCl at 18% and cleaned for removing excess of acid; then, the decarbonized material was
159 embedded in thin pellets and analyzed with Elemental Analyzer Flash2000 (Thermo Fisher) at the University
160 of Milan.

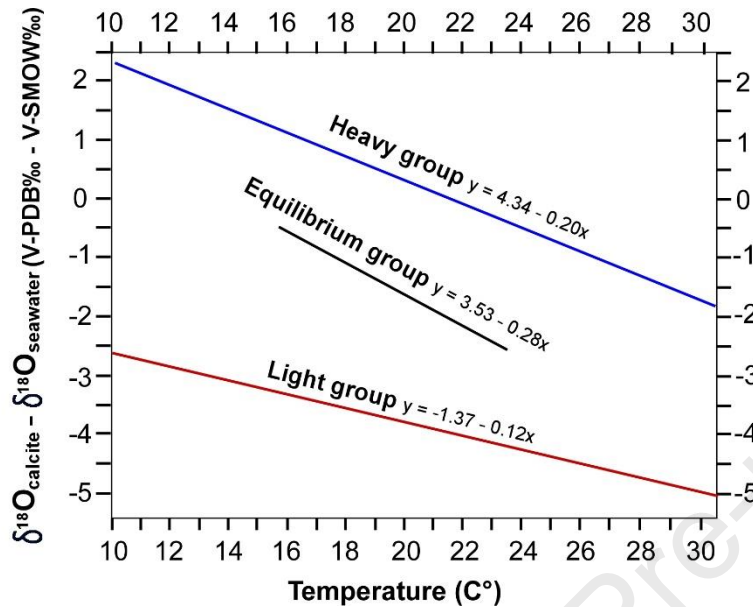
161 Ten powdered samples were processed with the X-Ray Powder Diffraction (XRPD) (Fig. 2) at the University
162 of Turin. The phase composition was determined by X-ray Powder Diffraction measurements using a para-
163 focusing geometry Rigaku Miniflex 600, with Cu-K α incident radiation and operating at 40 kV–15 mA. The
164 diffractometer is equipped with a DTex 250 detector and an optic configuration consisting of a fixed
165 divergence slit ($1/2^\circ$) and an anti-scatter slit ($1/2^\circ$). XRPD patterns were collected on powdered samples
166 between 3° and $70^\circ 2\theta$, with a 2θ -step size of 0.01 and scan speed of $1^\circ/\text{min}$, using a side-loading zero-
167 background sample holder. The phase content was inferred by Rietveld analysis, using high-purity ZnO as
168 an internal standard (10 wt%). Data refinements were carried out by the software GSAS-II (Toby and Von
169 Dreele, 2013). The Rietveld strategy involved the refinement of 15 Chebyshev polynomial background
170 coefficients, 2θ -zero parameter, cell parameters, phase fractions, isotropic crystal size, isotropic microstrain
171 of each phase and preferential orientation Mach-Dollase coefficients, when necessary. The PDF-4 2020
172 database enabled the phase identification.

173 3.2 Salinity reconstruction

174 $\delta^{18}\text{O}$ of biogenic calcite are a function of the temperature and the oxygen isotopic composition of seawater
175 (usually referred to as $\delta^{18}\text{O}_{\text{sw}}$) in which calcite precipitates. In living coccolithophores, the fractionation
176 factor for oxygen isotopes between water and calcite shows a large temperature dependence (Dudley et

177 al., 1986; Steinmetz, 1994; Hermoso, 2014). However, because of the “vital effect” on isotopic
178 fractionation, different taxa show a $\delta^{18}\text{O}$ offset with respect to the isotopic composition expected from
179 equilibrium fractionation during the precipitation of calcite at a given temperature (Dudley et al., 1986;
180 Hermoso, 2014; Fig. 3). For this reason, Dudley et al. (1986) and Hermoso, (2014) coined the terms “heavy
181 group”, “equilibrium group” and “light group” to describe the oxygen isotope departure from the
182 equilibrium of different taxa. Based on the assumption that most of the calcite in the analyzed samples
183 derives from well-preserved calcareous nanofossils (see Result section), the $\delta^{18}\text{O}$ values were converted
184 into sea surface salinity (SSS) by using different paleotemperature equations and applying the alkenone-
185 based sea surface temperature (SST) estimation provided by Tzanova et al. (2015) on the same section.
186 Being the alkenone a by-product of certain calcareous nanofossil taxa, the $\delta^{18}\text{O}_{\text{nanofossils}}$ is preferable over
187 $\delta^{18}\text{O}_{\text{foraminifers}}$ for the salinity evaluation, because it reduces inconsistency between proxy sources, such as
188 differences in the habitat of the living organism. To take into account the vital effect of different calcareous
189 nanofossils, we applied the paleotemperature equation of “heavy” ($y = 4.34 - 0.20x$), “equilibrium”
190 (approximated by *Helicosphaera carteri*: $y = 3.53 + 0.28x$) and “light” ($y = -1.37 - 0.12x$) coccolithophore
191 groups according to Dudley et al. (1986) and Ziveri et al. (2003), where y is $\delta^{18}\text{O}_{\text{calcite}} - \delta^{18}\text{O}_{\text{sw}}$ (‰ V-PDB – ‰
192 V-SMOW) and x is the temperature in °C (Fig. 3). Successively, we calculated the average between the 3
193 equations along with standard deviation in order to account the possible contribution of nanofossils with
194 different vital effect. In all equations, the SST was derived from the values provided by Tzanova et al.
195 (2015), which were recalculated to accommodate the different sampled stratigraphic levels by linear
196 interpolation using the sapropel mid-point as tie-points (insolation maxima; Hilgen et al., 2003) and
197 applying a constant sedimentation rate. The extrapolated SST and the calculated age for each sample are
198 reported in Tab 1. Finally, by removing the temperature influence on $\delta^{18}\text{O}_{\text{calcite}}$, we achieved $\delta^{18}\text{O}_{\text{sw}}$.
199 Changes in the continental ice volume also affect the global $\delta^{18}\text{O}_{\text{sw}}$, therefore it is necessary to estimate the
200 contribution of this component to obtain regional salinity change indications (Vasiliev et al., 2019;
201 Kontakiotis et al., 2022; Pilade et al., 2023). With this aim, we accounted for the change in the global ice
202 volume by correcting the $\delta^{18}\text{O}_{\text{sw}}$ with the Messinian record of sea-level change (Miller et al., 2011) and
203 applying a 0.008‰ increase per meter of sea level lowering (Siddal et al., 2003); successively, this value was
204 subtracted from the $\delta^{18}\text{O}_{\text{sw}}$ to obtain the regional ice volume free $\delta^{18}\text{O}_{\text{sw}}$ ($\delta^{18}\text{O}_{\text{ivf-sw}}$). The $\delta^{18}\text{O}$ value was
205 then converted to absolute SSS using the modern $\delta^{18}\text{O}_{\text{sw}}$ – salinity relationship for the Mediterranean Sea
206 ($\delta^{18}\text{O}_{\text{sw}} = 0.41 * \text{SSS} - 14.18$) (Kallel et al., 1997). However, the obtained SSS should be considered with
207 caution, as this conversion was calibrated for a narrow salinity range ($\sim 35\text{‰} - 39\text{‰}$) (Kallel et al., 1997) and
208 the assumed constant relationship between SSS and $\delta^{18}\text{O}_{\text{sw}}$ changed in the past (LeGrande and Schmidt,
209 2011), especially during the Messinian, which was characterized by large variations in freshwater input and
210 evaporation. In view of all these uncertainties, our SSS reconstructions are intended as an estimation of
211 salinity trend and presented for illustrative and comparative scope.

212 From the SSS and SST estimates, the density variation of the surface water was calculated assuming
 213 constant pressure according to the international thermodynamic equation of seawater [(d = d (Sa, t, p)),
 214 where Sa is the absolute salinity, t is the measured temperature and p is the pressure of seawater
 215 (Intergovernmental Oceanographic Commission, 2015).



216
 217 Fig. 3: Plot of $\delta^{18}\text{O}_{\text{calcite}} - \delta^{18}\text{O}_{\text{seawater}}$ versus the growth temperature of different coccolith taxa grouped according to their vital effect
 218 behavior. Light and heavy groups are defined by Dudley et al. (1986), and the equilibrium by Ziveri et al. (2003) and Hermoso,
 219 (2014).

220

221

222 4-Results

223 4.1 Sedimentological, petrographic, and micropaleontological features

224 The studied succession is typified by a cyclic stacking pattern. The cycles were usually described as couplets
 225 (Hüsing et al., 2009; Di Stefano et al., 2010); however, detailed field observations revealed that a packstone
 226 layer occurs between the marly limestone/marlstone and the sapropels (Figs. 2 and 5). The calcareous
 227 nannofossil assemblage in the quantitatively analyzed samples is dominated by *Umbilicosphaera jafari*,
 228 with a relative percentage spanning from 48% to 98% (Fig. 4). The full calcareous nannofossil assemblage is
 229 reported in the supplementary materials.

230

231 4.1.1 Packstone

232 This lithology forms thin (1-4 cm thick) brown/dark layers composed of sand-sized foraminifers and green
 233 minerals attributable to glauconite (Fig. 5), while the matrix is represented by carbonate mud mixed with
 234 clay. The base of each layer is an erosional surface cutting the underlying sapropel. The lower part of the

235 layers is usually poorly cemented and grades into a strongly cemented limestone at the top (Fig. 5). Based
 236 on the petrographic and sedimentological features, 2 levels (A and B) can be distinguished from the base to
 237 the top:

238 -Level A is characterized by high contents of foraminifers associated with varying amounts of glauconite
 239 (Fig. 5). The tests of foraminifers are consistently filled with sparry calcite (Fig. 4), with different
 240 cathodoluminescence brightness (bright orange) with respect to the matrix (non-luminescent brown) (Fig.
 241 5) due to a different trace element (Mn, Fe) content, pointing to different phases of precipitation.

242 -Level B is characterized by a pervasive bioturbation. The burrows are 0.5 to 5 mm in diameter, oriented
 243 parallel to the bedding, and filled with pyrite, barite, calcite and gypsum.

244 4.1.2 Marly limestone/marlstone

245 Based on the percentage of calcite (see paragraph 4.2), the whitish/grey layers interbedded with the
 246 sapropel are either marly limestone or marlstone (Fig. 2). These beds span from 7 to 20 cm in thickness and
 247 are usually laminated, showing the alternation of grey-white and brown-dark laminae (Fig. 5). The white
 248 laminae are 150 – 600 μm thick and are composed of closely packed fecal pellets (average size $\sim 200 \mu\text{m}$)
 249 rich in calcareous nannofossils (Figs. 4, 5 and 6). In some beds (i.e. cycles 253 and 254) fecal pellets are
 250 made of monospecific or oligospecific calcareous nannofossil assemblages of the taxon *U. jafari*. Pyrite and
 251 terrigenous grains (the latter only in cycles 255 and 256) are also present as minor components (Fig. 5). The
 252 brown-dark laminae mostly consist of fine-grained terrigenous material and pyrite grains (Fig. 5), as
 253 revealed by EDS analysis. Calcareous nannofossils are instead less abundant compared with the grey-white
 254 lamina. The foraminifer assemblage is dominated by poorly preserved benthic foraminifers filled with
 255 sparry calcite of diagenetic origin (Figs. 5 and 6).

256

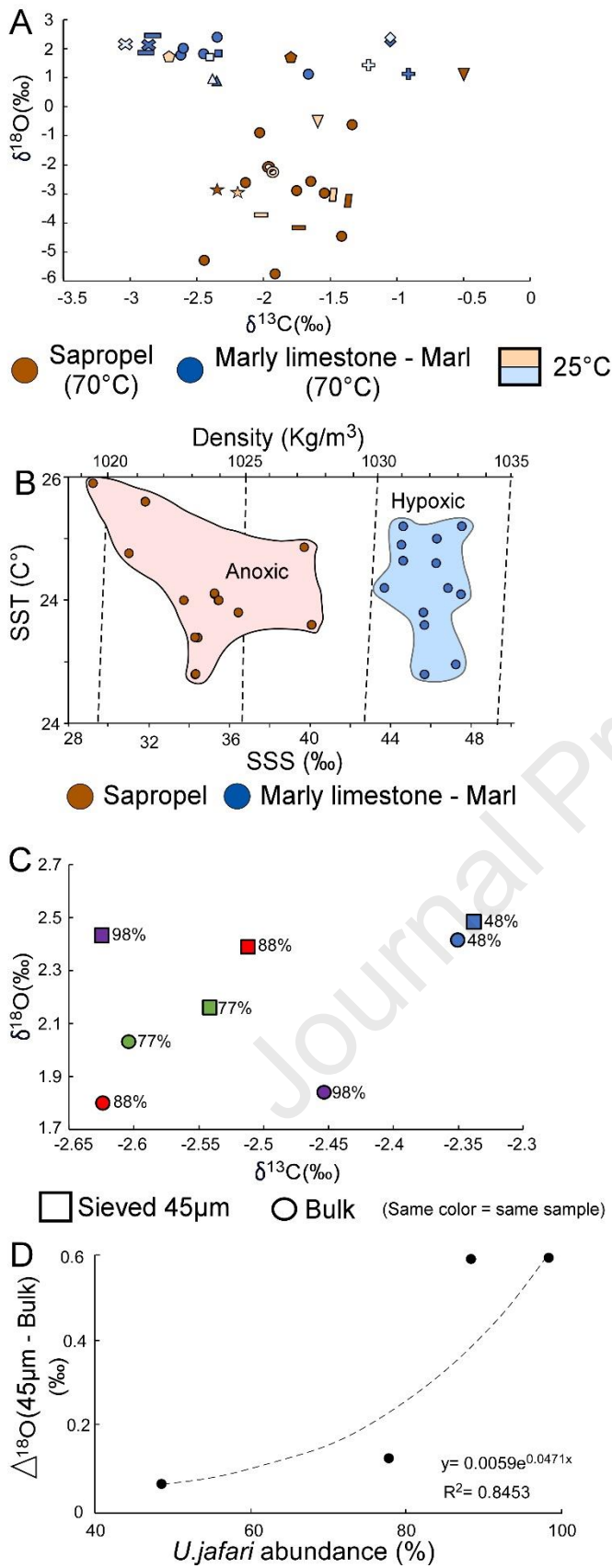
Age (kyr)	SST (C°)	$\delta^{18}\text{O}_{\text{bulk}}$ (‰)	$\delta^{18}\text{O}_{\text{sw}}$ (‰)				Sea level	$\delta^{18}\text{O}_{\text{ivf-sw}}$ (‰)	Sum St. dev.	SSS (‰)	St. dev.	Density (Kg/m ³)
			Heavy group	Equilibrium group	Light group	Average 3 groups						
6479.3	25.1	0.8	1.6	4.4	5.3	3.7 ± 1.6	-4.0	3.7	1.6	43.7 ± 4.7	4.7	1029.89 ± 2.92
6479.9	25.45	1.1	1.9	4.8	5.6	4.1 ± 1.6	-4.21	4.1	1.6	44.5 ± 4.7	4.7	1030.44 ± 2.91
6484.8	25.05	-2.6	-1.9	0.9	1.8	0.3 ± 1.6	-4.6	0.3	1.6	35.2 ± 4.7	4.7	1023.52 ± 2.91
6489.7	24.4	-2.9	-2.3	0.5	1.5	-0.1 ± 1.6	-3.8	-0.1	1.6	34.3 ± 4.7	4.7	1022.99 ± 2.93
6491.9	24.7	-2.9	-2.2	0.5	1.5	-0.1 ± 1.6	-4.7	-0.1	1.6	34.4 ± 4.7	4.7	1022.99 ± 2.92
6495.7	25.32	1.2	1.9	4.8	5.6	4.1 ± 1.6	-5.0	4.1	1.6	44.6 ± 4.7	4.7	1030.54 ± 2.92
6497.8	25.6	2.3	3.1	6.0	6.8	5.3 ± 1.6	-6.1	5.3	1.6	47.5 ± 4.7	4.7	1032.67 ± 2.91
6504.9	25.43	-0.9	-0.1	2.8	3.6	2.1 ± 1.6	-8.0	2.1	1.6	39.7 ± 4.7	4.7	1026.78 ± 2.91
6510.7	24.8	-0.6	0.1	2.9	3.8	2.3 ± 1.6	-8.4	2.2	1.6	40.1 ± 4.7	4.7	1027.25 ± 2.93
6512.8	24.9	1.7	2.4	5.2	6.1	4.5 ± 1.6	-8.45	4.5	1.6	45.6 ± 4.7	4.7	1031.44 ± 2.93
6514.9	25.05	2.4	3.1	5.9	6.8	5.3 ± 1.6	-4.9	5.3	1.6	47.5 ± 4.7	4.7	1032.81 ± 2.93
6517.0	25.3	1.9	2.6	5.4	6.3	4.8 ± 1.6	-4.9	4.8	1.6	46.3 ± 4.7	4.7	1031.79 ± 2.92

6520.0	25.6	1.1	1.9	4.8	5.6	4.1 ± 1.6	-4.98	4.1	1.6	44.6 ± 4.7	4.7	1030.45 ± 2.91
6521.0	25.71	-5.7	-4.9	-2.0	-1.2	-2.7 ± 1.6	-5.0	-2.7	1.6	28.0 ± 4.7	4.7	1017.81 ± 2.88
6527.4	25.95	-5.3	-4.4	-1.5	-0.7	-2.2 ± 1.6	-4.9	-2.2	1.6	29.2 ± 4.7	4.7	1018.70 ± 2.87
6529.4	25.8	-4.2	-3.3	-0.4	0.3	-1.1 ± 1.6	-4.0	-1.1	1.6	31.8 ± 4.7	4.7	1020.63 ± 2.85
6531.6	25.1	2.2	2.9	5.7	6.6	5.03 ± 1.6	-3.0	5.0	1.6	46.8 ± 4.7	4.7	1032.31 ± 2.93
6534.0	24.48	2.5	3.0	5.8	6.8	5.2 ± 1.6	-1.0	5.2	1.6	47.2 ± 4.7	4.7	1032.81 ± 2.95
6534.8	24.4	1.8	2.4	5.1	6.1	4.6 ± 1.6	-1.2	4.6	1.6	45.7 ± 4.7	4.7	1031.65 ± 2.95
6537.7	24.9	-2.1	-1.4	1.4	2.3	0.8 ± 1.6	-2.6	0.8	1.6	36.4 ± 4.7	4.7	1024.46 ± 2.92
6539.3	25	-3.2	-2.5	0.3	1.2	-0.4 ± 1.6	-4.9	-0.4	1.6	33.7 ± 4.7	4.7	1021.62 ± 2.31
6544.1	25.38	-4.4	-3.6	-0.8	0.0	-1.5 ± 1.6	-8.5	-1.5	1.6	31.0 ± 4.7	4.7	1020.21 ± 2.89
6547.6	24.7	-3.0	-2.3	0.5	1.4	-0.1 ± 1.6	-9.3	-0.1	1.6	34.3 ± 4.7	4.7	1022.90 ± 2.92
6549.7	25	-2.6	-1.8	1.0	1.9	0.4 ± 1.6	-9.3	0.4	1.6	35.4 ± 4.7	4.7	1023.68 ± 2.91
6551.7	25.5	1.8	2.6	5.5	6.3	4.8 ± 1.6	-8.8	4.8	1.6	46.3 ± 4.7	4.7	1031.75 ± 2.91
6553.3	24.8	1.7	2.4	5.2	6.1	4.6 ± 1.6	-7.6	4.6	1.6	45.7 ± 4.7	4.7	1031.59 ± 2.94

257

258 Tab. 1: Results of the calculated SSS and surficial density (for detail, see paragraph 3.2) with the age of the samples, the
259 interpolation with the alkenone-based SST reconstruction (Tzanova et al., 2015), the global sea-level variation during the Messinian
260 (Miller et al., 2011), the calculated $\delta^{18}\text{O}_{\text{IV-SW}}$ and the propagated standard deviation accounted for different paleotemperature
261 equations used.

262



263

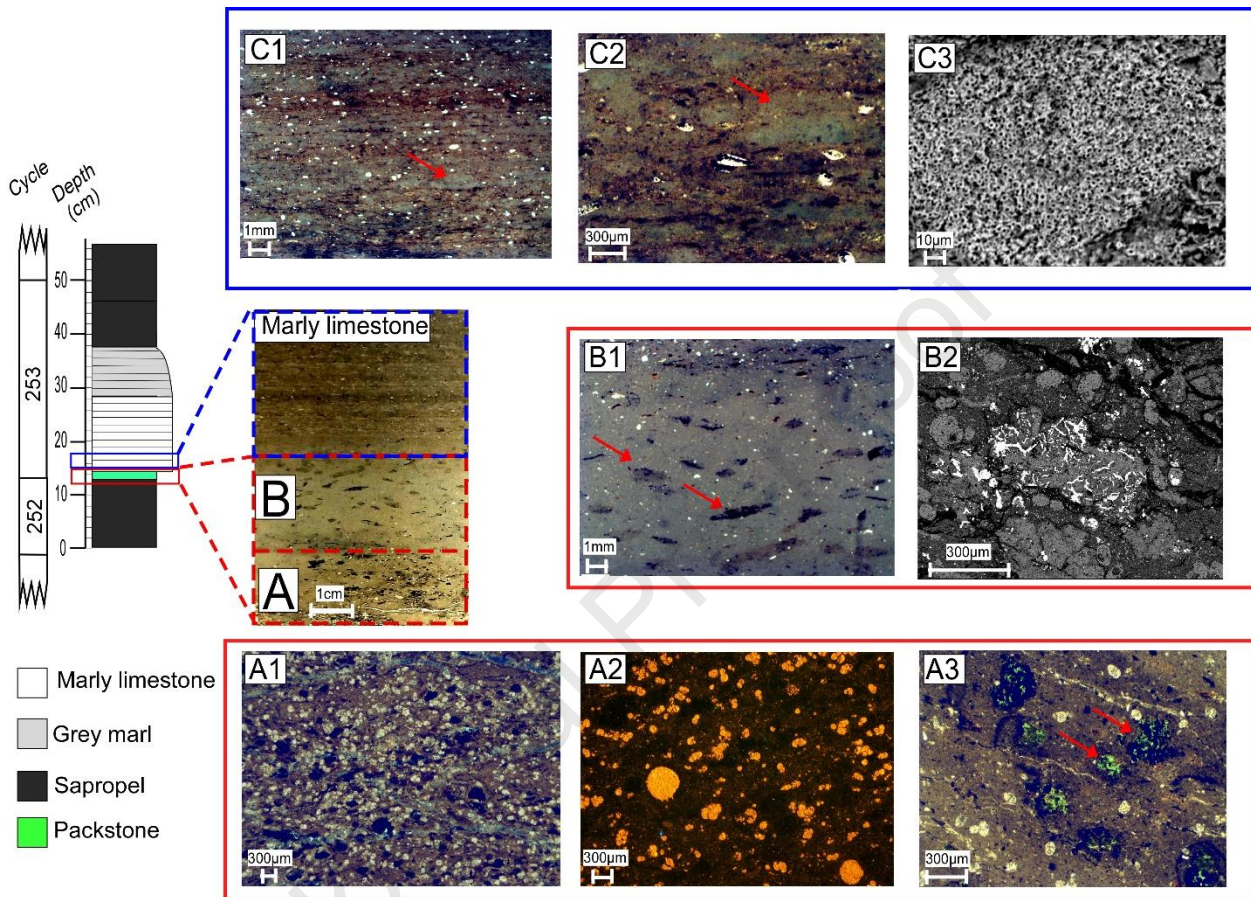
264 Fig. 4: Scattered plots of the measured $\delta^{13}\text{C}_{\text{calcite}}$, $\delta^{18}\text{O}_{\text{calcite}}$ values and *U. jafari* abundance.265 A: Plot showing the distribution of $\delta^{13}\text{C}_{\text{calcite}}$ and $\delta^{18}\text{O}_{\text{calcite}}$ values in different lithologies and with different procedures (treatment at
266 25° or 70°C). The same symbol refers to the same sample.

267 B: Density plot reconstructed from the SSS and SST of the different lithologies.

268 C: Comparison between the $\delta^{13}\text{C}$ and $\delta^{18}\text{O}$ values measured in the bulk sediment and sieved at $45\mu\text{m}$. Same color refers to same
 269 sample.

270 D: Plot showing the exponential relationship between the differences in the $\delta^{18}\text{O}_{45\mu\text{m}}$ and the $\delta^{18}\text{O}_{\text{bulk}}$ and the *U.jafari* relative
 271 abundance. The equation of the relationship and the linear relationship coefficient R^2 are shown in the right lower corner.

272



273

274 Fig.5: Thin section photomicrographs of the packstone to marly-limestone transition. Based on petrographic and sedimentological
 275 features, the packstone layer is divided into 2 distinct levels. Level A shows high abundance of foraminifers (A1 and A2) and
 276 glauconite (red arrows in A3). Note that the sparry calcite foraminifer infill shows a different luminescence with respect to the
 277 matrix when inspected with cathodoluminescence (A2). Level B is characterized by intense bioturbation (red arrows in B1). Burrows
 278 are filled with pyrite (B2). The marly limestone shows the alternation of whitish and brown laminae (C1 and C2). Whitish laminae
 279 are composed of fecal pellets with a monospecific calcareous nannofossil assemblage (red arrows in C1 and C2, magnified at the
 280 SEM in C3). A1, A3, B1, C1 and C2: optical microscope photomicrographs; A2: cathodoluminescence photomicrograph; B2 and C3:
 281 SEM photomicrographs.

282

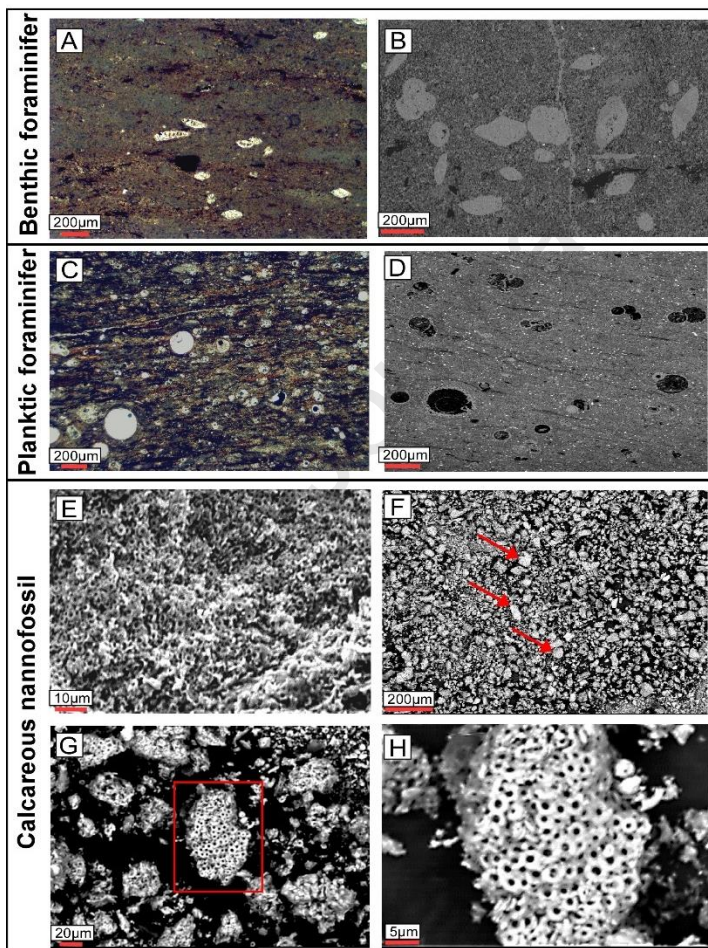
283 4.1.3 Sapropel

284 Sapropel layers are 20 to 50 cm thick and are finely laminated, with grey-white laminae (50 – 600 μm thick)
 285 mostly made up of peloids and fecal pellets, alternated with black-brown laminae (50 – 200 μm thick)
 286 composed of silt-sized terrigenous and pyrite grains. Foraminifers are scarce to abundant, and the
 287 assemblage is dominated by well-preserved planktic specimens, showing intact and well-preserved walls
 288 and empty chambers (Fig. 6). Calcareous nannofossils are less abundant compared to the marly
 289 limestone/marlstone samples.

290

291 **4.2 Mineralogy and geochemistry**

292 The mineralogical composition of the samples expressed in percentage is reported in Fig. 7. Overall, the
 293 marly limestone/marlstone shows higher calcite contents and lower pyrite, clay, and dolomite contents
 294 with respect to sapropel. The carbon and oxygen stable isotope analyses performed with acid digestion at
 295 25°C and 70°C show similar values (Fig. 4). The $\delta^{18}\text{O}$ values obtained at 70°C are consistently higher in the
 296 marly limestone/marlstone (from 0.8‰ to 2.4‰) and lower in the sapropel (from -5.7‰ to -0.6‰) (Fig. 7).
 297 The $\delta^{13}\text{C}$ values obtained at 70°C span from -2.8‰ to -0.5‰ (Fig. 7). The calcite fraction of the sieved
 298 samples is dominated by well-preserved calcareous nannofossils (Fig. 6). The sieved samples show similar
 299 $\delta^{18}\text{O}$ values of the bulk sediment samples (Fig. 5), with deviation in the range of 0.05‰ to 0.60‰ (Fig. 4).
 300 The TOC contents of the studied samples span from 0.9% to 3.1% (Fig. 7); on average the sapropel and the
 301 marly limestone/marlstone show TOC content of 2.0% and 0.8%, respectively.



302

303 Fig. 6: Photomicrographs of representative samples in transmitted light (A and C) and SEM (B, D, E, F, G and H).

304 A and B: Marly-limestone samples showing benthic foraminifers; calcite infill in the foraminifer chambers is visible.

305 C and D: Sapropel sample with planktic foraminifers.

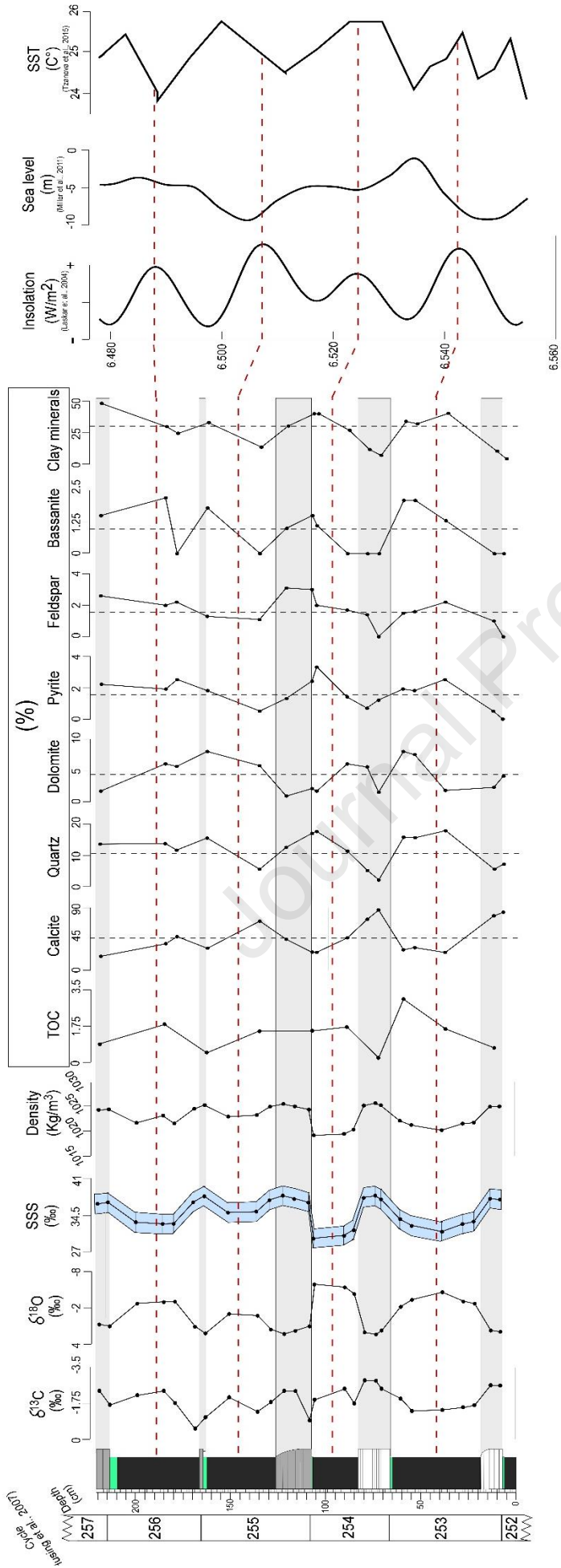
306 E: Freshly broken sediment chip showing fecal pellet composed of monospecific assemblage of *U. jafari*. F: Sample sieved at 45 μ m
307 (red arrows indicate the fecal pellets rich in calcareous nannofossils), G: Detail of F; the red square indicates the image in H. Note
308 the well-preserved calcareous nannofossil platelets.

309

310

311 4.3 The reconstructed $\delta^{18}\text{O}_{\text{SW}}$ and SSS estimation

312 The calculated $\delta^{18}\text{O}_{\text{SW}}$ obtained using the different paleotemperature equations and the correlation
313 between sea level and SST changes are given in Tab. 1. The average of the $\delta^{18}\text{O}_{\text{IVF-SW}}$ spans from $-2.7 \pm 1.6\text{‰}$
314 to $5.3 \pm 1.6\text{‰}$, (Tab. 1) with higher values recorded in the marly/limestone-marlstone layers and lower
315 values in the sapropel. The calculated SSS spans from $28.0\text{‰} \pm 4.7\text{‰}$ (sapropel of cycle 254) to $47.5\text{‰} \pm$
316 4.7‰ (marlstone of cycle 255) and shows an evident cyclical pattern related to the lithology (Figs. 4 and 7).
317 Sapropel shows lower SSS values (average 34.1‰) than the marly limestone/marlstone (average 46.0‰)
318 (Fig. 7). The sapropel of cycle 255 shows higher SSS values with respect to the other cycles (Fig. 7). Long
319 term salinity trend was not observed in the studied interval. The calculated surface water density spans
320 from $1017.8 \pm 2.9 \text{ Kg/m}^3$ to $1032.8 \pm 2.9 \text{ Kg/m}^3$, showing a similar trend and pattern of the SSS, with lower
321 values in the sapropel (average 1023.8 Kg/m^3) and higher values in the marly limestone/marlstone (average
322 1031.7 Kg/m^3) (Fig. 4).



324 Fig. 7: Geochemical, mineralogical, stable oxygen and carbon isotope and SSS results and their relationship with the insolation
325 curve at 45°N (Laskar et al., 2004), the global Sea level variation (Miller et al., 2011) and the alkenone-based SST measured at the
326 Monte dei Corvi section (Tzanova et al., 2015). Vertical dashed dark lines refer to the average values, while the horizontal dashed
327 red lines refer to the sapropel mid-points.

328

329 5 Discussions

330 5.1 Isotopic signature of the bulk rock

331 A detailed temperature and salinity reconstruction was hampered by the poor preservation of foraminifers
332 in the marly limestone/marlstone samples. Since the isotopic signature of the bulk rock can be biased by
333 the diagenetic calcite crystals filling and encrusting the foraminifer calcite tests (Fig. 6) (Zarkogiannis et al.,
334 2020), to obtain reliable reconstructions we compared the isotopic composition of bulk sediment with that
335 of calcareous nannofossils. The bulk $\delta^{18}\text{O}$ signature represents an averaged measure of all the different
336 carbonate components present in the sediment (e.g. foraminifers, calcareous nannofossils, abiogenic
337 calcite, dolomite, etc.). The obtained results then vary depending on the different calcite sources, which
338 have distinct $\delta^{18}\text{O}$ offsets (Turpin et al., 2011). Dolomite, which can be characterized by different isotopic
339 values with respect to calcite (Dela Pierre et al., 2012), is present in low abundance in the analyzed
340 samples. However, the $\delta^{18}\text{O}$ values obtained through the treatment with phosphoric acid at 25°C or 70°C
341 are similar (Fig. 4), suggesting that the $\delta^{18}\text{O}$ variations between marly limestone/marlstone and sapropel
342 are not related to fluctuations in the dolomite contents (dolomite fully reacts with acid only at 70°C;
343 Chaduteau et al., 2021). Diagenetic calcite crystals are rare in the sapropel, and only scattered in the marly
344 limestone/marlstone samples where they fill foraminifer chambers (Fig. 6). Nevertheless, for these marly
345 limestone/marlstone samples, we excluded the possible diagenetic bias of secondary calcite filling the
346 foraminifers by analyzing the calcite fraction <45 μm , which is mostly composed of well-preserved
347 nannofossils (Fig. 6).

348 The $\delta^{18}\text{O}$ values of calcareous nannofossils have been considered a more reliable proxy than the $\delta^{18}\text{O}$ of
349 planktic foraminifers for reconstructing seawater temperature and $\delta^{18}\text{O}_{\text{sw}}$ changes (Anderson and
350 Steinmetz, 1981). In fact, differently from planktic foraminifers, calcareous nannoplankton only proliferate
351 within the photic zone. They do not undergo vertical migration and calcification at various depths, and their
352 calcite platelets are more resistant to dissolution and less prone to recrystallization (Steinmetz, 1994;
353 Subhas et al., 2018). Furthermore, previous studies showed that the $\delta^{18}\text{O}_{\text{nannofossils}}$ covaried systematically
354 with the $\delta^{18}\text{O}_{\text{foraminifers}}$ during glacial-interglacial cycles, but with larger fluctuation amplitude, thus
355 demonstrating the greater sensitivity of calcareous nannofossils for paleoceanographic studies (Margolis et
356 al., 1975; Anderson and Steinmetz, 1981; Dudley and Nelson, 1989).

357 In order to test if the isotopic compositions of bulk calcite and of the calcareous nannofossils are
358 comparable, the difference between the bulk and sieved samples was calculated. Furthermore, we
359 compared the obtained differences between the bulk and calcareous nannofossils $\delta^{18}\text{O}$ values with the
360 diversity of calcareous nannofossil assemblages, expressed in % of *U. jafari* over the whole assemblage (Fig.
361 4) to highlight a possible bias originating from the different vital effects, characterizing different nannofossil
362 taxa. We show that the $\Delta^{18}\text{O}$ ($\delta^{18}\text{O}_{\text{sieved}} - \delta^{18}\text{O}_{\text{bulk}}$) is positively correlated with *U. jafari* relative abundance
363 ($R^2 = 0.8453$; Fig. 4); in other words, the isotopic difference between the sieved and bulk samples is lower as
364 nannofossil diversity increases. This suggests that when the calcareous nannofossil assemblage is
365 diversified, the bulk analysis reflects the calcareous nannofossil isotopic signature (0.06 ‰; Fig. 4); when
366 the calcareous nannofossil assemblage is monospecific (>88% of the assemblage is composed by one taxon)
367 this difference is higher (0.6‰) but anyway negligible when compared with the significant isotopic shift
368 characterizing our cyclic record (Fig. 7). Indeed, the $\delta^{18}\text{O}$ oscillations observed from sapropel to marly
369 limestone/marlstone are large (in some cases up to 7‰, and on average 3.3‰) and they cannot be solely
370 explained by the different calcareous nannofossil assemblage carrying different isotopic offset. Therefore,
371 the $\delta^{18}\text{O}_{\text{bulk}}$ variation between marly limestone/marlstone and sapropel represents a pristine signal
372 reflecting temperature and salinity changes in the upper water column, where the calcareous
373 nannoplankton proliferate.

374

375 5.2 The sedimentary expression of the thermohaline circulation change

376 The cyclic sedimentary stacking pattern observed in the analyzed section suggests recurrent changes in the
377 oceanographic conditions of the Adriatic Basin during the Messinian.

378 The erosional contacts at the base of each packstone layer, which is sandwiched between sapropel and
379 marly limestone/marlstone, indicate a hiatus. Level A is most likely the product of intense winnowing of the
380 seafloor by bottom currents (Giresse, 2008), which washed away the fine-grained fraction leaving the
381 sediment enriched in the sand-sized fraction at the seafloor. Prolonged sediment starvation in response to
382 intense winnowing favored the formation of glauconite (Giresse, 2008), which is abundant in level A. These
383 lines of evidence suggest that the packstone layers record the winnowing of the sea floor following intense
384 bottom current activity.

385 The intense bioturbation of Level B suggests an oxygenated seafloor, probably favored by the resumption
386 of thermohaline-driven bottom currents linked to precessional cyclicity. Therefore, we infer that the
387 maximum strength of the bottom current coincides with the erosional surface at the bottom of level A,
388 whereas the overlying parts record its slowing down.

389 The marly limestone/marlstone intervals exhibit frequent lamination, with occasional burrows and
390 abundant benthic foraminifers. Specifically, the benthic foraminifer community is primarily composed of
391 elongated biserial and triserial taxa (Iaccarino et al., 2008; Di Stefano et al., 2010), which are adapted to
392 thrive in oxygen-depleted environments with high carbon supply to the seafloor. Notably, bolivinids,
393 buliminids and uvigerinids (Murray, 2006; Schumacher et al., 2007) are prominent among these taxa. The
394 reduced oxygen levels in this setting have led to intermittent crises in the benthic ecosystem, allowing only
395 benthic foraminifers capable of tolerating sub-oxic bottom conditions to survive. These conditions also
396 favored the preservation of undisturbed lamination.

397 The sapropel layers suggest a further reduction in the bottom oxygen content, which is highlighted by the
398 decrease in abundance of benthic foraminifers, the complete absence of bioturbation, and higher pyrite
399 and terrigenous contents compared with the marly limestone/marlstone (Fig. 7). The small size (<10 μm) of
400 pyrite grains suggests anoxic conditions also in the water column (Bond and Wignall, 2010), because pyrite
401 tends to sink when it reaches this size range. The relatively high abundance of terrigenous minerals in the
402 sapropel is likely linked to increased runoff. These observations suggest that sapropels record the
403 weakening, or even the stopping, of the thermohaline circulation related to enhanced runoff, as already
404 proposed for other Messinian sapropel deposits in the Eastern Mediterranean (Schenau et al., 1999;
405 Gennari et al., 2018).

406

407 **5.3 The causes of the deoxygenation in the Adriatic Basin during the Messinian**

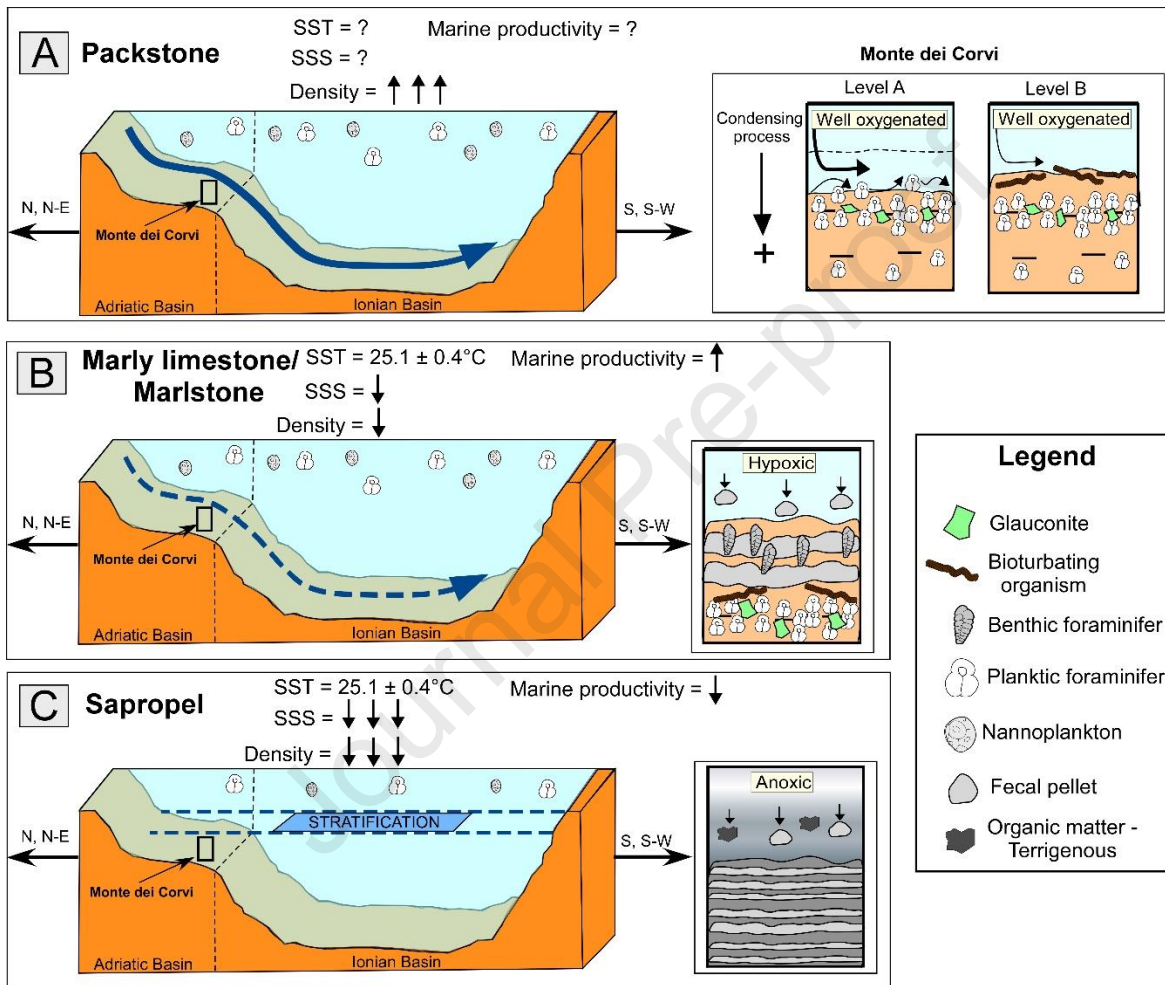
408 Nowadays, the Eastern Mediterranean deep-sea oxygenation is provided by the North Adriatic Deep Water
409 formation system, which mostly relies on the winter cold wind promoting a density gain of surficial waters,
410 their sinking and thus an efficient transport of oxygen to the bottom. The Messinian deep-water renewal
411 system of the Adriatic Basin and Eastern Mediterranean is supposed to have been similar to the modern
412 one (Kouwenhoven and van der Zwaan, 2006). After 6.7 Ma there is evidence of thermohaline circulation
413 weakening in response to the tectonic restriction of the Atlantic gateways (Kouwenhoven et al., 2003;
414 Sierro et al., 2003; Bulian et al., 2022), leading to enhanced sapropel formation. Instead, to the best of our
415 knowledge, the cyclical occurrence of packstone layers related to intense bottom current activity has never
416 been reported in the pre-evaporitic Messinian succession of the Adriatic Basin (Kouwenhoven et al., 1999;
417 Manzi et al., 2007). In this perspective, the Monte dei Corvi section was probably located in a strategic site,
418 intercepting the paleo-North Adriatic Deep-water path and therefore, recording variations in its strength.
419 Despite the absolute values of the obtained SSS should be taken with caution because they can be affected
420 by a large uncertainty (see paragraph 3.2), the obtained trend is reliable and allows to investigate the
421 behavior of the thermohaline circulation during the Messinian. Our SSS evaluation shows that sapropels
422 were deposited on average with SSS of 35.6‰ and with SST of 25.1°C (Fig. 7). The corresponding surface

423 water density estimation spans from 1017.8 to 1027.3 Kg/m³ (average 1023.8 Kg/m³) (Tab. 1). Thus, these
424 values are retained as indicative of the suppression of bottom water formation and consequent oxygen
425 delivery to the sea floor, allowing the preservation of organic-rich sediments (Fig. 8). The density values
426 during sapropel formation (Fig. 4) are lower than those of the modern Mediterranean, which is on average
427 1028 Kg/m³ (Droghei et al., 2018), and 1029.2 Kg/m³ in the Adriatic Sea (Gačić et al., 2001); these values
428 allow deep-water formation events. Therefore, if in the near future under the influence of global warming,
429 surface density values become similar to the Messinian sapropel, thermohaline circulation is likely to be
430 negatively affected, possibly resulting in the establishment of bottom anoxic conditions. Based on the
431 reconstructed SST and SSS, the Messinian sapropel deposition at Monte dei Corvi was mostly controlled by
432 variation in SSS (Tab. 1 and Fig. 7). This was probably related to increasing freshwater input into the basin in
433 response to precession-driven climatic and oceanographic changes. Furthermore, the sensitivity of the
434 Mediterranean Basin to freshwater input (hence SSS variation) was enhanced in response to the decreasing
435 amount of Atlantic water entering through the paleo Gibraltar Strait.

436 Noteworthy, another important parameter in the consumption of oxygen at the seafloor is the
437 remineralization of pelagic rain of organic carbon (Burdige, 2007; Keeling et al., 2010). The amount of
438 organic carbon reaching the sea floor depends on a wide array of factors (e.g. oxygen content,
439 remineralization and sedimentation rate, type of organic matter, etc.; Burdige, 2007); among them, the
440 surface primary productivity exerts the most important role. The Quaternary and Pliocene sapropels are
441 thought to have been deposited under the joint effect of the deterioration of the thermohaline circulation
442 and of an increase in marine productivity, both provided by enhanced river runoff from the Nile River
443 (Triantaphyllou et al., 2009; Hennekam et al., 2014; Athanasiou et al., 2017; Blanchet et al., 2021). Although
444 our dataset does not allow for a quantitative assessment of marine productivity, from a
445 micropaleontological and sedimentological perspective it can be inferred that the high abundance of fecal
446 pellets, primarily composed of monospecific and/or oligospecific nannofossil taxa (*U. jafari*) in the marly
447 limestone/marlstone layers, is indicative of enhanced primary productivity in the water column, with
448 subsequent export to the seafloor. A similar interpretation of *U. jafari* paleoecological preference was
449 proposed also for other Messinian sedimentary successions from the Mediterranean region (e.g., Lozar et
450 al., 2018; Pellegrino et al., 2020).

451 In contrast, such evidence is absent in the sapropel layers, suggesting that their deposition was
452 characterized by lower primary productivity and export in comparison to the marly limestone/marlstone
453 layers. It is important to note that the deposition of the marly limestone/marlstone layers occurred under
454 higher surface water density conditions compared to present-day conditions (Tab. 1). This higher density
455 would have facilitated effective renewal of oxygen at the bottom consequently, the hypoxic conditions
456 inferred from the marly limestone/marlstone layers can be attributed to enhanced productivity and
457 subsequent export to the seafloor, which promotes high consumption of oxygen during organic matter

458 remineralization. Such reconstruction suggests that primary productivity and export played a significant
 459 role in regulating the oxygen budget at the seafloor during the deposition of the marly
 460 limestone/marlstone layers. Conversely, the deposition of the sapropel layers was predominantly
 461 influenced by a weakening of the thermohaline circulation, resulting from the freshening of the upper part
 462 of the water column.
 463



464

465 Fig. 8: Sketch showing a N-NE to SSW oriented section of the Adriatic and Ionian basins with the main oceanographic processes
 466 characterizing the deposition of the different lithologies. The main sedimentary features at Monte dei Corvi are shown in the right
 467 panels. The blue arrows represent the Adriatic Deep Water formation system with the reconstructed SST and the deduced SSS and
 468 density of surface water (this work; Tzanova et al., 2015).

469

470 5.4 The Messinian deoxygenation dynamics: insight for the end of this century

471 Understanding past anoxic events is pivotal to tackle the future evolution of the marine environment in a
 472 global context of climate change. Indeed, the results obtained in this study testify the negative
 473 repercussions of reduced bottom oxygen levels on the seafloor ecosystem, a condition that is currently
 474 occurring in several marine sites (Diaz and Rosenberg, 2008). Seafloor deoxygenation not only involves the

475 disappearance of complex (i.e. multicellular) organisms in the lower part of the water column and at the
476 sediment/water interface, but likely affects also the biocenosis proliferating in the upper water column, as
477 observed in modern environments where hypoxic/anoxic conditions establish on the seafloor (Roman et
478 al., 2019 and references therein). As a modern example, in Elefsina Bay (Eastern Mediterranean), the
479 development of seasonal hypoxic zone at the bottom reduces the trophic transfer energy toward the
480 surface, thus impacting the plankton structure and favoring picoeukaryotes over mesozooplankton
481 (Batziakas et al., 2020), hence influencing the zooplankton and fish stock (Roman et al., 2019).

482 The Messinian record can provide clues to better understand some of the current deoxygenation cases as it
483 was characterized by the progressive restriction of the Mediterranean Basin in response to a reduced
484 connection with the Atlantic Ocean through the paleo-Gibraltar Strait (Kouwenhoven et al., 1999); these
485 conditions caused the excellent record of environmental change in the Mediterranean sedimentary
486 succession (Kouwenhoven et al., 2003; Mancini et al., 2020), especially for the variation in the thermohaline
487 circulation regime (Kouwenhoven and van der Zwaan, 2006). Indeed, the SST and SSS play a major role in
488 controlling the density of water and, therefore, on the thermohaline circulation strength. However,
489 modeling the future thermohaline circulation behavior based on SSS and SST is complicated. Although
490 there is a general consensus on the weakening of thermohaline circulation at the end of this century
491 (Somot et al., 2006; Planton et al., 2012; Powley et al., 2016), some studies show that this behavior
492 depends on the imposed boundary conditions, such as the river runoff flux (Adloff et al., 2015). Therefore,
493 it is crucial to establish the boundary conditions at the sea surface affecting thermohaline circulation and,
494 consequently, bottom deoxygenation. In this perspective, the Messinian sedimentary record of the
495 Mediterranean region is ideal to constrain the boundary condition (SST and SSS threshold) involved in the
496 deterioration of the thermohaline circulation strength under extreme paleoceanographic stress.

497 The climatic conditions during the Messinian represent a valuable analog for the next future scenario
498 because of similar SST. The SST recorded in the Eastern Mediterranean during the studied interval spans
499 from 22°C to 30°C (Mayser et al., 2017; Vasiliev et al., 2019; Kontakiotis et al., 2022; Butiseacă et al., 2022),
500 and from 24.4°C to 25.7°C in the Monte dei Corvi section (Tzanova et al., 2015) (Tab. 2). The SST ranges are
501 attributed to variation in the available insolation driven by precession. These values are higher than the
502 modern ones, which span from 17°C to 19°C in the period 1986-2015 in the Northern Adriatic, and from
503 20°C to 22.5°C in the Levantine and Ionian seas (Sakalli, 2017). However, using linear black box model, the
504 SST predicted for the period 2071-2100 (20°C – 21°C in the Northern Adriatic; 23°C - 26°C in the Levantine
505 and Ionian seas; Sakalli, 2017) is close to the range of the SST reconstructed for the Messinian from 6.6 –
506 6.4 Ma in the Eastern Mediterranean (Tzanova et al., 2015; Mayser et al., 2017; Vasiliev et al., 2019;
507 Kontakiotis et al., 2022; Butiseacă et al., 2022).

508 Predictions based on Regional Climate System Models, on multi-scenario emission approach, show that
509 with “business as usual” greenhouse gases emission (Representative Concentration Pathways 8.5, referred
510 to as RCP8.5 scenario), the SST will be in the range of 20.1°C – 22.3°C in the Northern Adriatic, and between
511 22.5°C – 25.9°C in the Levantine and Ionian seas at the end of this century (Darmaraki et al., 2019). The
512 general warming trend will be accompanied by increasing surface salinity, on average of 0.48 psu for the
513 whole Mediterranean (Somot et al., 2006). The comparison of the Messinian SST (Tzanova et al., 2015) and
514 the reconstructed SSS with the projected values for the end of this century in the Adriatic Sea show that the
515 boundary conditions for bottom deoxygenation in response to reduced thermohaline circulation strength
516 will not be reached. This is mostly because the projected increase in SSS counteracts the density loss by
517 warming (Somot et al., 2006). Furthermore, the freshwater input from the Nile River, which was the main
518 driver for the surface water buoyancy loss during past deoxygenation events (Rohling et al., 2015), almost
519 stopped after the building of the Aswan dam (Rohling and Bryden, 1992). This apparently suggests that,
520 sapropels will not be deposited on the Mediterranean seafloor in the next future in response to a reduced
521 density of the surface water. Nevertheless, it is important to consider that the deep-water renewal system
522 in the Eastern Mediterranean essentially relies on cold wind blowing during winter (Rohling et al., 2015);
523 thus, the thermohaline circulation strength and the deep-water renewal system are also controlled by the
524 winter SST in the Northern Adriatic and Levantine seas, although the role of the Aegean Sea could be
525 relevant in certain conditions (Roether et al., 1996; Incarbona et al., 2016). The resolution of our study
526 (century/millennia) is not sufficient to evidence interannual variability and seasonal variations, like for
527 instance the heatwaves phenomena. In the modern setting, heatwaves are currently increasing and are
528 predicted to further increase in the Mediterranean Basin (Darmaraki et al., 2019; Garrabou et al., 2022) and
529 could severely affect the thermohaline circulation, especially if they occur in winter. Furthermore, the
530 weakening of the thermohaline circulation is occurring simultaneously with coastal eutrophication, which is
531 contributing to oxygen depletion in various marginal sites within the Mediterranean (Diaz and Rosemberg,
532 2008). Although continental runoff is expected to decrease even further in the near future (Somot et al.,
533 2006), the flushing of water in the marine realm remains nutrient-rich due to anthropogenic inputs (Diaz
534 and Rosemberg, 2008). These substances can stimulate marine primary productivity, leading to oxygen loss.
535 If this fertilization of the marine environment extends to distal areas, the resulting oxygen consumption
536 from this process could be significant also in the deep-water setting. Therefore, all these additional forcing
537 should be also considered in the model-based projection of the Mediterranean oxygen balance, and a
538 hypoxic future of the Mediterranean cannot be excluded.

539

540

541

Reference	SST (C°)	Site	Proxy
	From 6.6 to 6.4 Ma		
Butiseacă et al., 2022	27.2 - 30	Agios Myron (Greece)	TEX ₈₆ ; U ₃₇ ^k
Kontakiotis et al., 2022	27.2 - 30	Agios Myron (Greece)	TEX ₈₆ ; U ₃₇ ^k
Mayser et al., 2017	22 - 29.8	Pissouri (Cyprus)	TEX ₈₆
Vasiliev et al., 2019	22 - 23.4	Kalamaki (Greece)	U ₃₇ ^k
Tzanova et al., 2015	24.0 - 26.0	Monte dei Corvi (Italy)	U ₃₇ ^k
/	From 2071 - 2100	/	Model
Sakalli, 2017	20 - 21	Northern Adriatic	Black box model
Sakalli, 2017	23 - 26	Levantine and Ionian	Black box model
Darmaraki et al., 2019	20.1 - 22.3	Northern Adriatic	Regional climate system (RCP8.5)
Darmaraki et al., 2019	22.5 - 25.9	Levantine and Ionian	Regional climate system (RCP8.5)

542

543 Tab. 2: Sea surface temperature recorded in the Eastern Mediterranean during the Messinian (~6.6 – 6.4Ma) and the projected SST
544 from 2071-2100 period.

545

546 Conclusions

547 During the Messinian, the Monte dei Corvi section was located in or near the Adriatic Deep Water
548 formation site and recorded variations in its intensity. Indeed, the lithological alternation made up of
549 packstone, marly limestone/marlstone and sapropel, reflects variation in the Adriatic Deep Water
550 formation system. The packstone layers overlying the sapropel beds were deposited under protracted
551 bottom current activities and represent the (precession-induced) cyclical maximum strength of the
552 thermohaline circulation, which resulted in the periodical restoration of a well-oxygenated bottom
553 environment. As testified by the benthic foraminifer assemblage, the marly limestone/marlstone was
554 deposited under bottom hypoxic conditions, which diminished the proliferation of bioturbating organisms.
555 The sapropels are characterized by the absence of bioturbation and scarce benthic foraminifers, thus
556 reflecting an ecological crisis affecting the deep ecosystem due to anoxic conditions.

557 Anoxic conditions during sapropel deposition were not primarily related to an intensification of marine
558 productivity but were achieved with an increase in the buoyancy of the surficial water mass, primarily
559 promoted by a decrease in the SSS, which in turn weakened the thermohaline circulation strength and
560 promoted bottom anoxic conditions.

561 Through a comparison of the Messinian climatic and oceanographic conditions with the projected scenarios
562 for the end of this century in the Mediterranean Basin, this study suggests that the seafloor will continue to
563 receive sufficient oxygen due to the compensatory effect of the increased SSS, which counteracts the
564 density loss caused by warming. Despite this, an evaluation of the role of primary productivity and

565 heatwaves is necessary for providing reliable forecasts of the oxygen balance fluctuations in marine
566 environments in the next future.

567

568 **Acknowledgment**

569 This project was supported by CRT (Cassa Risparmio Torino) grant 2021.0907 awarded to Francesca Lozar.

570 **1. References**

- 571 2. Adloff, F., Somot, S., Sevault, F., Jordà, G., Aznar, R., Déqué, M., Herrmann, M., Marcos, M., Dubois,
572 M., Padorno, E., Alvarez-Fanjul, E., Gomis, D., 2015. Mediterranean Sea response to climate change
573 in an ensemble of twenty first century scenarios. *Climate Dynamics*, 45, 2775-2802.
- 574 3. Anderson, T. F., Steinmetz, J. C., 1981. Isotopic and biostratigraphical records of calcareous
575 nanofossils in a Pleistocene core. *Nature*, 294, 741-744.
- 576 4. Athanasiou, M., Bouloubassi, I., Gogou, A., Klein, V., Dimiza, M. D., Parinos, C., Skampa, E.,
577 Triantaphyllou, M. V., 2017. Sea surface temperatures and environmental conditions during the
578 “warm Pliocene” interval (~ 4.1–3.2 Ma) in the Eastern Mediterranean (Cyprus). *Global and*
579 *planetary change*, 150, 46-57.
- 580 5. Athanasiou, M., Triantaphyllou, M. V., Dimiza, M. D., Gogou, A., Panagiotopoulos, I., Arabas, A.,
581 Skampa, e., Kouli, M., Tsiolakis, E., 2021. Reconstruction of oceanographic and environmental
582 conditions in the eastern Mediterranean (Kottafi Hill section, Cyprus Island) during the middle
583 Miocene Climate Transition. *Revue de micropaléontologie*, 70, 100480.
- 584 6. Batziakas, S., Frangoulis, C., Tsiola, A., Nikolioudakis, N., Tsagaraki, T. M., & Somarakis, S., 2020.
585 Hypoxia changes the shape of the biomass size spectrum of planktonic communities: A case study in
586 the eastern Mediterranean (Elefsina Bay). *Journal of Plankton Research*, 42, 752-766.
- 587 7. Blanchet, C. L., Tjallingii, R., Schleicher, A. M., Schouten, S., Frank, M., Brauer, A., 2021.
588 Deoxygenation dynamics on the western Nile deep-sea fan during sapropel S1 from seasonal to
589 millennial timescales. *Climate of the Past*, 17, 1025-1050.
- 590 8. Bond, D. P., Wignall, P. B., 2010. Pyrite framboid study of marine Permian–Triassic boundary
591 sections: a complex anoxic event and its relationship to contemporaneous mass
592 extinction. *Bulletin*, 122, 1265-1279.
- 593 9. Bulian, F., Kouwenhoven, T. J., Jiménez-Espejo, F. J., Krijgsman, W., Andersen, N., Sierro, F. J., 2022.
594 Impact of the Mediterranean-Atlantic connectivity and the late Miocene carbon shift on deep-sea
595 communities in the Western Alboran Basin. *Palaeogeography, Palaeoclimatology,*
596 *Palaeoecology*, 589, 110841.
- 597 10. Burdige, D. J., 2007. *Geochemistry of marine sediments*. Princeton university press.

- 598 11. Butiseacă, G.A., van der Meer, M.T.J., Kontakiotis, G., Agiadi, K., Thivaïou, D., Besiou, E.,
599 Antonarakou, A., Mulch, A., Vasiliev, I., 2022. Multiple Crises Preceded the Mediterranean Salinity
600 Crisis: Aridification and Vegetation Changes Revealed by Biomarkers and Stable Isotopes. *Global and*
601 *Planetary Change*, 217, 103951.
- 602 12. Chaduteau, C., Ader, M., Lebeau, O., Landais, G., Busigny, V., 2021. Organic matter removal for
603 continuous flow isotope ratio mass spectrometry analysis of carbon and oxygen isotope
604 compositions of calcite or dolomite in organic-rich samples. *Limnology and Oceanography:*
605 *Methods*, 19, 523-539.
- 606 13. Darmaraki, S., Somot, S., Sevault, F., Nabat, P., Cabos-Narvaez, W. D., Cavicchia, L., Djurdjevic, V., Li,
607 L., Sannino, G., Sein, D. V., 2019. Future evolution of marine heatwaves in the Mediterranean Sea.
608 *Climate Dynamics*, 53, 1371-1392.
- 609 14. De Lange, G. J., Thomson, J., Reitz, A., Slomp, C. P., Speranza Principato, M., Erba, E., Corselli, C.,
610 2008. Synchronous basin-wide formation and redox-controlled preservation of a Mediterranean
611 sapropel. *Nature Geoscience*, 1, 606-610.
- 612 15. Dela Pierre, F., Clari, P., Bernardi, E., Natalicchio, M., Costa, E., Cavagna, S., Lozar, F., Lugli, S., Manzi,
613 V., Roveri, M., Violanti, D., 2012. Messinian carbonate-rich beds of the Tertiary Piedmont Basin (NW
614 Italy): microbially-mediated products straddling the onset of the salinity crisis. *Palaeogeography,*
615 *Palaeoclimatology, Palaeoecology*, 344, 78-93.
- 616 16. Di Stefano, A., Verducci, M., Lirer, F., Ferraro, L., Iaccarino, S. M., Hüsing, S. K., Hilgen, F. J., 2010.
617 Paleoenvironmental conditions preceding the Messinian Salinity Crisis in the Central Mediterranean:
618 integrated data from the Upper Miocene Trave section (Italy). *Palaeogeography, Palaeoclimatology,*
619 *Palaeoecology*, 297, 37-53.
- 620 17. Diaz, R. J., Rosenberg, R., 2008. Spreading dead zones and consequences for marine
621 ecosystems. *Science* 321, 926-929.
- 622 18. Droghei, R., Buongiorno Nardelli, B., Santoleri, R., 2018. A new global sea surface salinity and density
623 dataset from multivariate observations (1993–2016). *Frontiers in Marine Science*, 5, 84.
- 624 19. Dudley, W. C., Blackwelder, P., Brand, L., Duplessy, J. C., 1986. Stable isotopic composition of
625 coccoliths. *Marine micropaleontology*, 10, 1-8.
- 626 20. Dudley, W. C., Nelson, C. S., 1989. Quaternary surface-water stable isotope signal from calcareous
627 nanofossils at DSDP Site 593, southern Tasman Sea. *Marine Micropaleontology*, 13, 353-373.
- 628 21. Flecker, R., Krijgsman, W., Capella, W., de Castro Martins, C., Dmitrieva, E., Mayser, J.P., Marzocchi,
629 A., Modestou, S., Ochoa, D., Simon, D., Tulbure, M., van den Berg, B., van der Schee, M., de Lange,
630 G., Ellam, R., Govers, R., Gutjahr, M., Hilgen, F., Kouwenhoven, T., Lofi, J., Meijer, P., Sierro, F.J.,
631 Bachiri, N., Barhoun, N., Alami, A.C., Chacon, B., Flores, J.A., Gregory, J., Howard, J., Lunt, D., Ochoa,
632 M., Pancost, R., Vincent, S., Yousfi, M.Z., 2015. Evolution of the Late Miocene Mediterranean-

- 633 Atlantic gateways and their impact on regional and global environmental change. *Earth Science*
634 *Review* 150, 365-392.
- 635 22. Gačić, M., Lascaratos, A., Manca, B. B., Mantziafou, A., 2001. Adriatic deep water and interaction
636 with the Eastern Mediterranean Sea. In *Physical oceanography of the Adriatic Sea* (pp. 111-142).
637 Springer, Dordrecht.
- 638 23. Garrabou, J., Coma, R., Bensoussan, N., Bally, M., Chevalloné, P., Cigliano, M., Diaz, D., Harmelin,
639 J.G., Gambi, M.C., Kersting, D.K., Ledoux, J.B., Lejeusne, C., Linares, C., Marschal, C., Pérez, T., Ribes,
640 M., Romano, J.C., Serrano, E., Teixido, N., Torrents, O., Zabala, M., Zuberer, F., Cerrano, C., 2022.
641 Marine heatwaves drive recurrent mass mortalities in the Mediterranean Sea. *Global Change*
642 *Biology*, 28, 5708-5725.
- 643 24. Gennari, R., Lozar, F., Turco, E., Dela Pierre, F., Lugli, S., Manzi, V., Natalicchio, M., Roveri, M.,
644 Schreiber, B. C., Taviani, M., 2018. Integrated stratigraphy and paleoceanographic evolution of the
645 pre-evaporitic phase of the Messinian salinity crisis in the Eastern Mediterranean as recorded in the
646 Tokhni section (Cyprus island). *Newsletters on Stratigraphy*, 51, 33-55.
- 647 25. Giorgi, F., 2006. Climate change hot-spots. *Geophysical research letters*, 33, L08707.
- 648 26. Giresse, P., 2008. Some aspects of diagenesis in contourites. *Developments in sedimentology*, 60,
649 203-221.
- 650 27. Gladstone, R., Flecker, R., Valdes, P., Lunt, D., Markwick, P., 2007. The Mediterranean hydrologic
651 budget from a Late Miocene global climate simulation. *Palaeogeography, Palaeoclimatology,*
652 *Palaeoecology*, 25, 254-267.
- 653 28. Hennekam, R., Jilbert, T., Schnetger, B., de Lange, G. J., 2014. Solar forcing of Nile discharge and
654 sapropel S1 formation in the early to middle Holocene eastern Mediterranean. *Paleoceanography*,
655 29, 343-356.
- 656 29. Hermoso, M., 2014. Coccolith-derived isotopic proxies in palaeoceanography: where geologists need
657 biologists. *Cryptogamie, Algologie*, 35, 323-351.
- 658 30. Hilgen, F. J., Aziz, H. A., Krijgsman, W., Raffi, I., Turco, E., 2003. Integrated stratigraphy and
659 astronomical tuning of the Serravallian and lower Tortonian at Monte dei Corvi (Middle–Upper
660 Miocene, northern Italy). *Palaeogeography, Palaeoclimatology, Palaeoecology*, 199, 229-264.
- 661 31. Hüsing, S. K., Kuiper, K. F., Link, W., Hilgen, F. J., Krijgsman, W., 2009. The upper Tortonian–lower
662 Messinian at Monte dei Corvi (Northern Apennines, Italy): completing a Mediterranean reference
663 section for the Tortonian stage. *Earth and Planetary Science Letters*, 282, 140-157.
- 664 32. Iaccarino, S.M., Bertini, A., Di Stefano, A., Ferraro, L., Gennari, R., Grossi, F., Lirer, F., Manzi, V.,
665 Menichetti, E., Ricci Lucchi, M., Taviani, M., Sturiale, G., Angeletti, L., 2008. The Trave section
666 (Monte dei Corvi, Ancona, Central Italy): an integrated paleontological study of the Messinian
667 deposits. *Stratigraphy* 5, 281-306.

- 668 33. Incarbona, A., Martrat, B., Mortyn, P., Sprovieri, M., Ziveri, P., Gogou, A., Jord`a, A., Xoplaki, E.,
669 Luterbacher, J., Langone, L., Marino, G., Rodríguez-Sanz, L., Triantaphyllou, M., Di Stefano, E.,
670 Grimalt, J., Tranchida, G., Sprovieri, R., Mazzola, S., 2016. Mediterranean circulation perturbations
671 over the last five centuries: Relevance to past Eastern Mediterranean Transient-type
672 events. *Scientific Reports*, 6, 29623.
- 673 34. Intergovernmental Oceanographic Commission, 2015. The International thermodynamic equation of
674 seawater–2010: calculation and use of thermodynamic properties. [includes corrections up to 31st
675 October 2015].
- 676 35. IPCC. Climate Change 2021: The Physical Science Basis. Contribution of Working Group I to the Sixth
677 Assessment Report of the Intergovernmental Panel on Climate Change; Masson-Delmotte, V., Zhai,
678 P., Pirani, A., Connors, S.L., Péan, C., Berger, S., Caud, N., Chen, Y., Goldfarb, L., Gomis, M.I., et al.,
679 Eds.; Cambridge University Press: Cambridge, UK; New York, NY, USA.
- 680 36. Keeling, R. F., Körtzinger, A., Gruber, N., 2010. Ocean deoxygenation in a warming world. *Annual*
681 *Review of Marine Science*, 2, 199-229.
- 682 37. Kidd et al., 1978. Stratigraphy of eastern sapropel sequence recovered during DSDP leg 41 A and
683 their paleoenvironmental significance, *Initial Report Deep Sea Research*, 1, 421-443.
- 684 38. Kontakiotis, G., Butiseac̆a, G.-A., Karakitsios, V., Antonarakou, A., Zarkogiannis, S., Agiadi, K., Krsnik,
685 E., Besiou, E., Zachariasse, J.-W., Lourens, L., Thivaïou, D., Koskeridou, E., Moissette, P., Mulch, A.,
686 Vasiliev, I., 2022. Hypersalinity accompanies tectonic restriction in the eastern Mediterranean prior
687 to the Messinian Salinity Crisis. *Palaeogeography, Palaeoclimatology, Palaeoecology*, 592, 110903.
- 688 39. Kouwenhoven, T. J., Seidenkrantz, M. S., Van der Zwaan, G. J., 1999. Deep-water changes: the near-
689 synchronous disappearance of a group of benthic foraminifera from the Late Miocene
690 Mediterranean. *Palaeogeography, Palaeoclimatology, Palaeoecology*, 152, 259-281.
- 691 40. Kouwenhoven, T. J., Hilgen, F. J., Van der Zwaan, G. J., 2003. Late Tortonian–early Messinian
692 stepwise disruption of the Mediterranean–Atlantic connections: constraints from benthic
693 foraminiferal and geochemical data. *Palaeogeography, Palaeoclimatology, Palaeoecology*, 198, 303-
694 319.
- 695 41. Kouwenhoven, T. V., Van der Zwaan, G. J., 2006. A reconstruction of late Miocene Mediterranean
696 circulation patterns using benthic foraminifera. *Palaeogeography, Palaeoclimatology,*
697 *Palaeoecology*, 238, 373-385.
- 698 42. Lozar, F., Violanti, D., Bernardi, E., Dela Pierre, F., Natalicchio, M., 2018. Identifying the onset of the
699 Messinian salinity crisis: a reassessment of the biochronostratigraphic tools (Piedmont Basin, NW
700 Italy). *Newsletters on Stratigraphy*, 51, 11-31.

- 701 43. Mancini, A. M., Bocci, G., Morigi, C., Gennari, R., Lozar, F., Negri, A., 2023. Past Analogues of
702 Deoxygenation Events in the Mediterranean Sea: A Tool to Constrain Future Impacts. *Journal of*
703 *Marine Science and Engineering*, 11, 562.
- 704 44. Mancini, A. M., Gennari, R., Ziveri, P., Mortyn, P. G., Stolwijk, D. J., Lozar, F., 2020. Calcareous
705 nanofossil and foraminiferal trace element records in the Sorbas Basin: A new piece of the
706 Messinian Salinity Crisis onset puzzle. *Palaeogeography, Palaeoclimatology, Palaeoecology*, 554,
707 109796.
- 708 45. Manzi, V., Roveri, M., Gennari, R., Bertini, A., Biffi, U., Giunta, S., Iaccarino, S.M., Lanci, L., Lugli, S.,
709 Negri, A., Riva, A., Rossi, M.E., Taviani, M., 2007. The deep-water counterpart of the messinian lower
710 evaporites in the apennine foredeep: the fanantello section (northern Apennines, Italy).
711 *Palaeogeography, Palaeoclimatology, Palaeoecology*, 251, 470-499.
- 712 46. Margolis, S. V., Kroopnick, P. M., Goodney, D. E., Dudley, W. C., Mahoney, M. E., 1975. Oxygen and
713 carbon isotopes from calcareous nanofossils as paleoceanographic indicators. *Science*, 189, 555-
714 557.
- 715 47. Mayser, J. P., Flecker, R., Marzocchi, A., Kouwenhoven, T. J., Lunt, D. J., Pancost, R. D., 2017.
716 Precession driven changes in terrestrial organic matter input to the Eastern Mediterranean leading
717 up to the Messinian Salinity Crisis. *Earth and Planetary Science Letters*, 462, 199-211.
- 718 48. Miller, K. G., Mountain, G. S., Wright, J. D., Browning, J. V., 2011. A 180-million-year record of sea
719 level and ice volume variations from continental margin and deep-sea isotopic
720 records. *Oceanography*, 24, 40-53.
- 721 49. Murray, J. W. *Ecology and applications of benthic foraminifera*. Cambridge university press, 2006.
- 722 50. Pellegrino, L., Abe, K., Gennari, R., Lozar, F., Pierre, F. D., Natalicchio, M., Mikami, Y., Jordan, R. W.,
723 Carnevale, G., 2020. Integrated micropaleontological study of the Messinian diatomaceous deposits
724 of the Monferrato Arc (Piedmont basin, NW Italy): New insights into the paleoceanographic
725 evolution of the northernmost Mediterranean region. *Marine Micropaleontology*, 160, 101910.
- 726 51. Pilade, F., Vasiliev, I., Birgel, D., Pierre, F. D., Natalicchio, M., Mancini, A., Carnevale, G., Gennari, R.,
727 2023. Deciphering the termination of the Messinian salinity crisis: The alkenone record of the
728 Miocene-Pliocene transition in the northern Mediterranean. *Palaeogeography, Palaeoclimatology,*
729 *Palaeoecology*, 631, 111831.
- 730 52. Planton, S., Lionello, P., Artale, V., Aznar, R., Carrillo, A., Colin, J., Congedi, L., Dubois, C., Elizalde,
731 A., Gualdif, S., Hertigg, E., Jacobeit, J., Jordà, G., Li, Laurent, Mariotti, A., Piani, C., Ruti, P., Sanchez-
732 Gomez, E., Sannino, G., Sevault, F., Somot, S., Tsimplis, M., 2012. The climate of the mediterranean
733 region in future climate projections. In: *The Climate of the Mediterranean Region*. Elsevier, Oxford,
734 pp. 449-502.

- 735 53. Popov, S.V., Rogl, F., Rozanov, A.Y., Steininger, F.F., Shcherba, I.G., Kovac, M., 2004. Lithological-
736 paleogeographic maps of paratethys. *CFS Cour. Forschungsinstitut Senckenberg*, 254, 1-46.
- 737 54. Powley, H. R., Krom, M. D., Van Cappellen, P., 2016. Circulation and oxygen cycling in the
738 Mediterranean Sea: Sensitivity to future climate change. *Journal of Geophysical Research:*
739 *Oceans*, 121, 8230-8247.
- 740 55. Roether, W., Manca, B.B., Klien, B., Bregant, D., Georgopoulos, D., Beitzel, V., Kovacevic, V.,
741 Luchetta, A., 1996. Recent changes in Eastern Mediterranean deep waters. *Science*
742 271, 333–335.
- 743 54- Rohling, E. J., Bryden, H. L., 1992. Man-induced salinity and temperature increases in Western
744 Mediterranean Deep Water. *Journal of Geophysical Research: Oceans*, 97, 11191-11198.
- 745 55- Rohling, E.J., Marino, G., Grant, K.M., 2015. Mediterranean climate and oceanography, and the
746 periodic development of anoxic events (sapropels). *Earth-Science Review*, 143, 62-97.
- 747 56- Roman, M. R., Brandt, S. B., Houde, E. D., Pierson, J. J., 2019. Interactive effects of hypoxia and
748 temperature on coastal pelagic zooplankton and fish. *Frontiers in Marine Science*, 6, 139.
- 749 57- Rossignol-Strick, M., Nesteroff, W., Olive, P., Vergnaud-Grazzini, C., 1982. After the deluge:
750 Mediterranean stagnation and sapropel formation. *Nature*, 295, 105-110.
- 751 58- Roveri, M., Boscolo Gallo, A., Rossi, M., Gennari, R., Iaccarino, S.M., Lugli, S., Manzi, V., Negri, A.,
752 Rizzini, F., Taviani, M., 2005. The Adriatic foreland record of Messinian events (central Adriatic sea,
753 Italy). *GeoActa* 4, 158.
- 754 59- Roveri, M., Flecker, R., Krijgsman, W., Lofi, J., Lugli, S., Manzi, V., Sierro, F.J., Bertini, A., Camerlenghi,
755 A., De Lange, G., Govers, R., Hilgen, F.J., Hübscher, C., Meijer, P.T., Stoica, M., 2014. The Messinian
756 Salinity Crisis: past and future of a great challenge for marine sciences. *Marine Geology* 352, 25-58.
- 757 60- Sakalli, A., 2017. Sea surface temperature change in the Mediterranean Sea under climate change: a
758 linear model for simulation of the sea surface temperature up to 2100. *Applied Ecology and*
759 *Environmental Research*, 15, 707-716.
- 760 61- Schenau, S. J., Antonarakou, A., Hilgen, F. J., Lourens, L. J., Nijenhuis, I. A., Van der Weijden, C. H.,
761 Zachariasse, W. J., 1999. Organic-rich layers in the Metochia section (Gavdos, Greece): evidence for
762 a single mechanism of sapropel formation during the past 10 My. *Marine Geology*, 153, 117-135.
- 763 62- Schumacher, S., Jorissen, F. J., Dissard, D., Larkin, K. E., Gooday, A. J., 2007. Live (Rose Bengal
764 stained) and dead benthic foraminifera from the oxygen minimum zone of the Pakistan continental
765 margin (Arabian Sea). *Marine Micropaleontology*, 62, 45-73.
- 766 63- Siddall, M., Rohling, E.J., Almogi-Labin, A., Hemleben, Ch., Meischner, D., Schmelzer, I., Smeed, D.A.,
767 2003. Sea-level fluctuations during the last glacial cycle. *Nature*, 423, 853-858.
- 768 64- Sierro, F.J., Flores, J.A., Ba'rcena, M.A., Vazquez, A., Utrilla, R., Zamarreno, I., 2003. Orbitally-
769 controlled oscillations in the planktic communities and cyclical changes in western Mediterranean

- 770 hydrography during the Messinian. *Palaeogeography, Palaeoclimatology, Palaeoecology* 190, 289-
771 316.
- 772 65- Somot, S., Sevault, F., Déqué, M., 2006. Transient climate change scenario simulation of the
773 Mediterranean Sea for the twenty-first century using a high-resolution ocean circulation model.
774 *Climate Dynamics*, 27, 851-879.
- 775 66- Steinmetz, J. C., 1994. Stable isotopes in modern coccolithophores. *Coccolithophores*. Cambridge
776 University Press, Cambridge, 219-229.
- 777 67- Stratford, K., Williams, R. G., Myers, P. G., 2000. Impact of the circulation on sapropel formation in
778 the eastern Mediterranean. *Global Biogeochemical Cycles*, 14, 683-695.
- 779 68- Subhas, A. V., Rollins, N. E., Berelson, W. M., Erez, J., Ziveri, P., Langer, G., Adkins, J. F., 2018. The
780 dissolution behavior of biogenic calcites in seawater and a possible role for magnesium and organic
781 carbon. *Marine Chemistry*, 205, 100-112.
- 782 69- Taylforth, J. E., McCay, G. A., Ellam, R., Raffi, I., Kroon, D., Robertson, A. H., 2014. Middle Miocene
783 (Langhian) sapropel formation in the easternmost Mediterranean deep-water basin: Evidence from
784 northern Cyprus. *Marine and Petroleum Geology*, 57, 521-536.
- 785 70- Triantaphyllou, M.V., Ziveri, P., Gogou, A., Marino, G., Lykousis, V., Bouloubassi, I., Emeis, K.-C.,
786 Kouli, K., Dimizia, M., Rosell-Melé, A., Papanikolaou, M., Katsouras, G., Nunez, N., 2009. Late Glacial-
787 Holocene climate variability at the south-eastern margin of the Aegean Sea. *Marine Geology*, 266,
788 182-197
- 789 71- Toby, B. H., Von Dreele, R. B., 2013. GSAS-II: the genesis of a modern open-source all purpose
790 crystallography software package. *Journal of Applied Crystallography*, 46, 544-549.
- 791 72- Turpin, M., Emmanuel, L., Reijmer, J. J., Renard, M., 2011. Whiting-related sediment export along
792 the Middle Miocene carbonate ramp of Great Bahama Bank. *International journal of earth
793 sciences*, 100, 1875-1893.
- 794 73- Tzanova, A., Herbert, T. D., Peterson, L., 2015. Cooling Mediterranean Sea surface temperatures
795 during the Late Miocene provide a climate context for evolutionary transitions in Africa and
796 Eurasia. *Earth and Planetary Science Letters*, 419, 71-80.
- 797 74- Vasiliev, I., Karakitsios, V., Bouloubassi, I., Agiadi, K., Kontakiotis, G., Antonarakou, A.,
798 Triantaphyllou, M., Gogou, A., Kafousia, N., de Rafelis, M., Zarkogiannis, S., Kaczmar, F., Parinos, C.,
799 Pasadakis, N., 2019. Large sea surface temperature, salinity, and productivity preservation changes
800 preceding the onset of the Messinian Salinity Crisis in the eastern Mediterranean Sea.
801 *Paleoceanography and Paleoclimatology*, 34, 182-202.
- 802 75- Zarkogiannis, S. D., Kontakiotis, G., Gkaniatsa, G., Kuppili, V. S., Marathe, S., Wanelik, K., ...
803 Antonarakou, A., 2020. An improved cleaning protocol for foraminiferal calcite from unconsolidated

804 core sediments: HyPerCal—a new practice for micropaleontological and paleoclimatic
805 proxies. *Journal of Marine Science and Engineering*, 8, 998, 10.3390/jmse8120998.
806 76- Ziveri, P., Stoll, H., Probert, I., Klaas, C., Geisen, M., Ganssen, G., Young, J., 2003. Stable isotope ‘vital
807 effects’ in coccolith calcite. *Earth and planetary science letters*, 210, 137-149.

808

Journal Pre-proof

Highlights:

The Monte dei Corvi recorded the changes in the ADW formation during the Messinian

The bottom deoxygenation resulted from variations in the freshwater input

Future deoxygenation in Mediterranean can be provided by productivity or heatwaves

Journal Pre-proof

Conflicts of Interest:

The authors declare no conflict of interest.

Journal Pre-proof